Accretion disc cooling and narrow absorption lines in the tidal disruption event AT 2019dsg

Cannizzaro, G.; Wevers, T.; Jonker, P. G.; Pérez-Torres, M. A.; Moldon, J.; Mata-Sánchez, D.; Leloudas, G.; Pasham, D. R.; Mattila, S.; Arcavi, I.; French, K. Decker; Onori, F.; Inserra, C.; Nicholl, M.; Gromadzki, M.; Chen, T. -W.; Müller-Bravo, T. E.; Short, P.; Anderson, J. P.; Young, D. R.

DOI:
10.1093/mnras/stab851

Monthly Notices of the ROYAL ASTRONOMICAL SOCIETY

MNRAS **504,** 792–815 (2021) doi:10.1093/mnras/stab851
Advance Access publication 2021 March 24

Accretion disc cooling and narrow absorption lines in the tidal disruption event AT 2019dsg

G. Cannizzaro [1,2★] T. Wevers [3,4] P. G. Jonker,[1,2] M. A. Pérez-Torres,[5] J. Moldon,[5,6] D. Mata-Sánchez [6] G. Leloudas,[7] D. R. Pasham,[8] S. Mattila,[9] I. Arcavi,[10,11] K. Decker French,[12] F. Onori [13] C. Inserra [14] M. Nicholl,[15,16] M. Gromadzki [17] T.-W. Chen,[18] T. E. Müller-Bravo [19] P. Short [16] J. P. Anderson,[4] D. R. Young,[20] K. C. Gendreau,[21] Z. Arzoumanian,[21] M. Löwenstein,[21,22] R. Remillard,[8] R. Roy[23] and D. Hiramatsu[24,25]

[1]*SRON, Netherlands Institute for Space Research, Sorbonnelaan, 2, NL-3584CA Utrecht, the Netherlands*
[2]*Department of Astrophysics/IMAPP, Radboud University, PO Box 9010, NL-6500 GL Nijmegen, the Netherlands*
[3]*Institute of Astronomy, University of Cambridge, Madingley Road, Cambridge CB3 0HA, UK*
[4]*European Southern Observatory, Alonso de Córdova 3107, Casilla 19, Santiago, 7550000, Chile*
[5]*Instituto de Astrofísica de Andalucía (CSIC), Glorieta de la Astronomía s/n, E-18080 Granada, Spain*
[6]*Jodrell Bank Centre for Astrophysics, School of Physics and Astronomy, The University of Manchester, Manchester M13 9PL, UK*
[7]*DTU Space, National Space Institute, Technical University of Denmark, Elektrovej 327, 2800 Kgs. Lyngby, Denmark*
[8]*MIT Kavli Institute for Astrophysics and Space Research, Cambridge, MA 02139, USA*
[9]*Tuorla Observatory, Department of Physics and Astronomy, University of Turku, FI-20014, Turku, Finland*
[10]*The School of Physics and Astronomy, Tel Aviv University, Tel Aviv 69978, Israel*
[11]*CIFAR Azrieli Global Scholars program, CIFAR, Toronto, ON M5G 1M1 Canada*
[12]*Department of Astronomy, University of Illinois, Urbana, IL 61801, USA*
[13]*INAF - Osservatorio Astronomico d'Abruzzo via M. Maggini snc, I-64100 Teramo, Italy*
[14]*School of Physics & Astronomy, Cardiff University, Queens Buildings, The Parade, Cardiff CF24 3AA, UK*
[15]*Birmingham Institute for Gravitational Wave Astronomy and School of Physics and Astronomy, University of Birmingham, Birmingham B15 2TT, UK*
[16]*Institute for Astronomy, University of Edinburgh, Royal Observatory, Blackford Hill EH9 3HJ, UK*
[17]*Astronomical Observatory, University of Warsaw, Al. Ujazdowskie 4, PL-00-478 Warszawa, Poland*
[18]*The Oskar Klein Centre, Department of Astronomy, Stockholm University, AlbaNova, SE-10691 Stockholm, Sweden*
[19]*School of Physics and Astronomy, University of Southampton, Southampton, Hampshire SO17 1BJ, UK*
[20]*Astrophysics Research Centre, School of Mathematics and Physics, Queens University Belfast, Belfast BT7 1NN, UK*
[21]*Astrophysics Science Division, NASA Goddard Space Flight Center, Greenbelt, MD 20771, USA*
[22]*Department of Astronomy, University of Maryland, College Park, MD 20742, USA*
[23]*The Inter-University Centre for Astronomy and Astrophysics, Ganeshkhind, Pune 411007, India*
[24]*Las Cumbres Observatory, 6740 Cortona Drive, Suite 102, Goleta, CA 93117-5575, USA*
[25]*Department of Physics, University of California, Santa Barbara, CA 93106-9530, USA*

Accepted 2021 March 16. Received 2021 March 9; in original form 2020 October 22

ABSTRACT

We present the results of a large multiwavelength follow-up campaign of the tidal disruption event (TDE) AT 2019dsg, focusing on low to high resolution optical spectroscopy, X-ray, and radio observations. The galaxy hosts a super massive black hole of mass $(5.4 \pm 3.2) \times 10^6\,M_\odot$ and careful analysis finds no evidence for the presence of an active galactic nucleus, instead the TDE host galaxy shows narrow optical emission lines that likely arise from star formation activity. The transient is luminous in the X-rays, radio, UV, and optical. The X-ray emission becomes undetected after ∼100 d, and the radio luminosity density starts to decay at frequencies above 5.4 GHz by ∼160 d. Optical emission line signatures of the TDE are present up to ∼200 d after the light-curve peak. The medium to high resolution spectra show traces of absorption lines that we propose originate in the self-gravitating debris streams. At late times, after ∼200 d, narrow Fe lines appear in the spectra. The TDE was previously classified as N-strong, but after careful subtraction of the host galaxy's stellar contribution, we find no evidence for these N lines in the TDE spectrum, even though O Bowen lines are detected. The observed properties of the X-ray emission are fully consistent with the detection of the inner regions of a cooling accretion disc. The optical and radio properties are consistent with this central engine seen at a low inclination (i.e. seen from the poles).

Key words: Accretion, accretion discs – galaxies: nuclei – transients: tidal disruption events.

★ E-mail: g.cannizzaro@sron.nl

1 INTRODUCTION

In the nuclear regions of a galaxy, a star whose orbital pericentre passes too close to the central supermassive black hole (SMBH) will be torn apart by the tidal forces (Hills 1975; Rees 1988; Evans & Kochanek 1989). During this so-called tidal disruption event (TDE), roughly half of the stellar matter will spiral towards the SMBH, confined into self-gravitating streams (Guillochon, Manukian & Ramirez-Ruiz 2014) that can self-intersect and dissipate energy. This phenomenon gives rise to a luminous flare, typically peaking in the ultraviolet (UV) or soft X-rays, which can exceed the Eddington luminosity of the SMBH, over time-scales of months to a year. While TDEs were originally discovered in the X-ray band (see Komossa 2002, for a review), recently significant numbers of TDE candidates are being discovered through wide field time domain optical surveys (e.g. Leloudas et al. 2016; Blagorodnova et al. 2017; Wyrzykowski et al. 2017; Holoien et al. 2018; Blagorodnova et al. 2019; Onori et al. 2019; van Velzen et al. 2020). The optical emission of TDEs has shown a wide variety of properties, but they are usually characterized by broad H and He emission lines (Arcavi et al. 2014), a strong blue continuum, blackbody (BB) temperatures of order 10^4 K and luminosities of order 10^{44} erg s^{-1}. A subset of TDEs have shown metal lines: either N and O lines (Blagorodnova et al. 2019; Leloudas et al. 2019; Onori et al. 2019) excited through the Bowen fluorescence mechanism (Bowen 1934, 1935) and/or low-ionization Fe lines (Wevers et al. 2019b). The presence/absence of H, He, and N lines led to the phenomenological classification of van Velzen et al. (2020) into three classes: TDE-H, TDE-He, and TDE-Bowen. There is no consensus on the origin of the optical emission of TDEs, be it either reprocessing of X-ray light through an atmosphere (Guillochon et al. 2014; Stone & Metzger 2016; Dai et al. 2018) or originating from shocks due to the self-intersections of the debris stream (Piran et al. 2015; Shiokawa et al. 2015; Bonnerot & Lu 2019).

While the presence of an accretion disc has been inferred also in optically selected TDEs, through the emergence of metal lines, double-peaked line profiles (Short et al. 2020; Hung et al. 2020), and their X-ray properties (Jonker et al. 2020; Wevers 2020), the TDE system has yet to be fully understood. This is hindered by the low numbers of TDE candidates (a few dozens), lack of high cadence, detailed spectroscopic monitoring, possible presence of reprocessing dust (Mattila et al. 2018), the presence of (non)-relativistic radio outflows (see Alexander et al. 2020, for a review), and/or the dependency on the viewing angle of the observed properties (Dai et al. 2018; Nicholl et al. 2019a).

We present the analysis of an intensive follow-up campaign of AT 2019dsg, a nuclear transient discovered on 2019 April 9 by the Zwicky Transfient Facility (ZTF; Nordin et al. 2019), with the name ZTF19aapreis and subsequently classified as a TDE, at a magnitude r = 18.9. The transient was discovered within a galaxy at a redshift z = 0.0512 (Nicholl et al. 2019b), which translates into a distance of D = 224 Mpc (we do not consider uncertainties in the luminosity distance), assuming a cosmology with $H_0 = 67.7$ km s^{-1} Mpc^{-1}, $\Omega_M = 0.309$, $\Omega_\Lambda = 0.691$ (Planck Collaboration 2014). In van Velzen et al. (2020), AT 2019dsg was studied as part of a larger sample of TDEs discovered by the ZTF. AT 2019dsg is categorized as a 'TDE-Bowen' due to the perceived presence of H Balmer, He II as well as Bowen (N/O) fluorescence lines (Bowen 1934, 1935). The host galaxy of AT 2019dsg is in the 'Green Valley' (Schawinski et al. 2014), a transition area of the colour-mass diagram between star-forming and quiescent galaxies. Galaxies in this region can show strong Balmer lines and the post-starburst, E+A galaxies, which are known to be preferential hosts for TDEs (Arcavi et al. 2014; French, Arcavi & Zabludoff 2016), are also in this region. AT 2019dsg was also listed as a candidate counterpart for a neutrino event (Stein et al. 2019a). A study of the possible neutrino emission from AT 2019dsg and a more detailed analysis of the spectral energy distribution (SED) is presented in Stein et al. (2020), where they propose a 'multizone' model to explain the various emission components of the transient: a central engine for the X-ray emission, an UV/Optical photosphere, and an outflow that powers the radio and neutrino emission. In this work, we focus on the X-ray emission and the optical spectra, on which we perform subtraction of the stellar component of the galaxy. Through this, we find that the N emission lines previously identified with the TDE are instead due to the host galaxy. Finally, in our medium and high resolution spectra, we find evidence for absorption lines, potentially due to the streams of disrupted stellar material. Throughout this manuscript, we use MJD 58603.1 as a reference date, which is the epoch at which the optical light curve peaks, as reported by van Velzen et al. (2020). All uncertainties are reported as 1σ, unless stated otherwise.

2 OBSERVATIONS

2.1 Swift UVOT/XRT

AT 2019dsg was observed with the UVOT and XRT instruments on board the Neil Gehrels *Swift* satellite (Gehrels et al. 2004) with a cadence of around 3 d starting on 2019 May 21 until 2019 Oct 15. We reduce and extract Swift/UVOT measurements using the UVOTSOURCE task in HEASOFT version 6.24. We use a standard 5 arcsec aperture to extract flux measurements, and a 50 arcsec aperture centred on an empty nearby region to estimate sky background levels. We correct for Galactic extinction assuming E(B−V) = 0.087 (Schlafly & Finkbeiner 2011).

We use the online Swift/XRT pipeline tool[1] to reduce the X-ray data and determine source count rates in the 0.3–10 keV band, using the source optical coordinates. Due to the low number of counts, we create a single stacked spectrum with a total exposure time of 20 ks for spectral analysis.

2.2 NICER

Following the *Swift* detection of X-rays from AT 2019dsg, the Neutron star Interior Composition ExploreR (*NICER*; Gendreau et al. 2016) made several observations between 2019 May 21 and 2019 June 6. A second set of observations were obtained several months later (2019 October 3–5) in response to the IceCube alert of a neutrino detection from a sky region containing AT 2019dsg (Stein et al. 2019b). All observations of AT 2019dsg (OBSIDs: 2006801010-2200680112) are reprocessed using the gain file *nixtiflightpi20170601v005.fits* by applying the NICERL2 FTOOL with the default filtering criteria.

To build up statistics, data from observation IDs 2200680103-2200680104 and 2200680107-2200680108 are combined due to observational proximity in time and/or short exposure times. Observation IDs 2200680110-2200680112 are also combined. The total spectra for these seven groups are extracted and the background spectra are estimated using empirical background spectral libraries, constructed from observations of source-free areas of sky.

[1] https://www.swift.ac.uk/user_objects/

Table 1. Spectroscopic observations.

MJD[(1)] (d)	Phase[(2)] (d)	UTC Date	Instrument	Exposure time (s)	Slit (arcsec)
58616.36	+13	2019 May 13	EFOSC2	900	1.0
58631.13	+28	2019 May 27	DOLORES	1800	1.5
58638.28	+35	2019 June 03	WFCCD	4 × 900	1.0
58642.35	+39	2019 June 08	EFOSC2	1800	1.0
58644.32	+41	2019 June 10	EFOSC2	2700	1.0
58655.19	+52	2019 June 20	ACAM	1800	0.75
58656.12	+53	2019 June 21	ACAM	1800	0.75
58657.09	+54	2019 June 22	ACAM	1800	0.75
58658.14	+55	2019 June 23	ACAM	1800	0.75
58668.22	+65	2019 July 04	UVES	1800	1.0
58676.19	+73	2019 July 12	ACAM	1800	1.0
58678.10	+75	2019 July 13	ACAM	2 × 1800	1.0
58689.25	+86	2019 July 25	EFOSC2	2700	1.0
58690.11	+87	2019 July 25	ACAM	1800	0.75
58692.12	+89	2019 July 27	ACAM	1800	1.0
58710.94	+108	2019 Aug 15	ACAM	1800	1.0
58715.88	+113	2019 Aug 20	ACAM	2 × 1800	1.0
58717.00	+114	2019 Aug 21	ACAM	5 × 1800	1.0
58717.89	+115	2019 Aug 22	ISIS	2 × 2700	1.0
58724.14	+121	2019 Aug 29	XSH/UVB	4 × 920	1.0
58724.14	+121	2019 Aug 29	XSH/VIS	4 × 920	0.9
58724.14	+121	2019 Aug 29	XSH/NIR	8 × 480	0.9
58733.93	+131	2019 Sept 07	ACAM	2 × 1800	1.0
58735.96	+133	2019 Sept 09	ACAM	2 × 1800	0.75
58777.02	+174	2019 Oct 10	EFOSC2	2 × 1800	1.5
58808.04	+205	2019 Nov 21	EFOSC2	2100	1.0
58824.83	+222	2019 Dec 07	ACAM	2200	1.5
58827.82	+224	2019 Dec 10	ACAM	2700	1.5
58994.12	+391	2020 May 24	DOLORES	2 × 2200	1.0

[(1)]Modified Julian Day of observations; [(2)]calculated with respect to the epoch of peak luminosity MJD 58603.1.

2.3 Optical spectroscopic observations

2.3.1 WHT/ISIS

Observations of AT 2019dsg were obtained with the Intermediate dispersion Spectrograph and Imaging System (ISIS) mounted at the Cassegrain focus of the William Herschel Telescope (WHT) in Roque de los Muchachos observatory (La Palma, Spain), Spain on 2019 August 22 under program SW19b01. Using a 1 arcsec slit in combination with the R600B grating provides wavelength coverage between 3600 and 5100 Å in the host rest frame, while the R600R grating covers the 6300–7800 Å range. The seeing was variable between 0.5 and 0.9 arcsec during the 2 × 2700 s observations, leading to a seeing limited full width half-maximum (FWHM) spectral resolution of ∼94 km s^{-1} (i.e. $\sigma_{instr} = 40$ km s^{-1}), measured at ∼4000 Å from the arc frame. The observations were carried out with the slit at parallactic angle (Filippenko 1982) and with binning 1×1.

After performing the standard reduction tasks, such as a bias level subtraction and flat-field correction, in IRAF (Tody 1986), we extract spectra using an extraction box with width of 1 arcsec in the spatial dimension. Wavelength solutions are applied using CuAr+CuNe arc frames obtained prior and after the science exposures. We combined the two exposures into a single, averaged spectrum using weights set to the average signal-to-noise ratio (SNR) of the individual spectra, and subsequently we fit cubic splines to normalize the averaged spectrum to the continuum (the spectra were not flux calibrated due to the absence of a standard star observation). A journal of the spectroscopic observations is presented in Table 1.

2.3.2 WHT/ACAM

AT 2019dsg was observed several times with the Auxiliary-port CAMera (ACAM) low-resolution spectrograph mounted at the Cassegrain focus of the WHT under program W19AN003. The V400 grating in combination with the GG395A order-sorting filter provides a wavelength coverage of 3950–9400 Å and the resolution is R∼430 and ∼580 for a 1.0 and 0.75 arcsec slit, respectively (from the technical manual of the instrument, measured at 5650 Å). The data were reduced using a pipeline based on standard IRAF data reductions procedures: flat-field and bias correction, cosmic ray cleaning, wavelength and flux calibration with arc lamps and standard stars. All observations were carried out with the slit at parallactic angle and with 1 × 1 binning.

2.3.3 TNG/DOLORES

We observed AT2019dsg twice with the Device Optimized for the LOw RESolution (DOLORES), installed at the Nasmyth B focus of the Telescopio Nazionale Galileo (TNG) in Roque de los Muchachos observatory (La Palma, Spain). The wavelength coverage of the LR-B grating is ∼3000–8430 Å, with a resolution R∼580 for a 1.0 arcsec slit (nominal value, measured at 5850 Å). The slit was oriented at parallactic angle for all observations and the binning was 1 × 1. The spectra were reduced using standard `iraf` procedures (bias and flat-field correction, wavelength, and flux calibration with arc lamps and standard stars).

2.3.4 NTT/EFOSC2

Observations of AT 2019dsg were carried out in the framework of the advanced Public ESO Spectroscopic Survey for Transient Objects (ePESSTO+; Smartt et al. 2015), starting with the classification spectrum taken on 2019 May 13 (Nicholl et al. 2019b), with the ESO Faint Object Spectrograph and Camera v.2 (EFOSC2), an instrument for low-resolution spectroscopy mounted at the Nasmyth B focus of the New Technology Telescope (NTT) at the La Silla observatory, Chile. All observations were performed using grism Gr#13, which provides a nominal wavelength coverage of 3685–9315 Å and a resolution with R∼355 for a 1 arcsec slit, measured at 5600 Å (nominal value), with the slit at parallactic angle and with 1 × 1 binning. Data were reduced using pipelines based on standard IRAF tasks, such as bias and flat-field correction, and wavelength and flux calibration using arc lamps and standard stars. When necessary, multiple spectra taken on the same night have been averaged with weights set to the mean value of the SNR of the individual exposures.

2.3.5 VLT/X-SHOOTER

We obtained one spectrum with the medium resolution spectrograph X-Shooter (Vernet et al. 2011), mounted at the Cassegrain focus of the second Unit Telescope (UT2) at the Very Large Telescope (VLT). X-shooter covers the wavelength range from 3000 to 25 000 Å. The observation was carried out on 2019 August 29 with slit widths of 1.0, 0.9, and 0.9 arcsec for the UVB, VIS, and NIR arms, respectively, with the slit oriented at parallactic angle. The set up used yields resolution of R ≃ 5400 (UVB), R ≃ 8900 (VIS), and R ≃ 5600 (NIR). The data were reduced using the REFLEX X-shooter pipeline version 2.9.3 (Freudling et al. 2013) and are not flux calibrated. The spectra were also corrected for atmospheric absorption features using synthetic transmission spectra with the MOLECFIT software (Smette

et al. 2015; Kausch et al. 2015). The NIR part of the spectrum shows no significant spectroscopic TDE signatures and is therefore not considered in this paper.

2.3.6 VLT/UVES

We observed AT 2019dsg with the Ultraviolet and Visual Echelle Spectrograph (UVES), mounted at the Nasmyth B focus of UT2 at the VLT. The observation was carried out on 2019 Jul 4 with the standard central wavelengths of 346 + 580 nm (dichroic 1) and 437 + 860 nm (dichroic 2) that provide an almost full coverage of the 300–1060 nm wavelength range. With a 1 arcsec slit, the resolving power is ∼40 000. The data were reduced using the UVES pipeline (Ballester et al. 2000), adjusting the pipeline parameters where necessary.

2.3.7 Las Cumbres/FLOYDS

Las Cumbres Observatory optical spectra were taken with the Folded Low Order whYte-pupil Double-dispersed Spectrograph (FLOYDS) mounted on the 2 m Faulkes Telescope North and South at Haleakala (USA) and Siding Spring (Australia), respectively. A 2 arcsec slit was placed on the target at the parallactic angle. One-dimensional spectra were extracted, reduced, and calibrated following standard procedures using the FLOYDS pipeline[2] (Valenti et al. 2014). The FLOYDS spectra are not used in the analysis, due to a combination of low SNR, wavelength range covered, and proximity in time with higher quality spectra. None the less, the spectra are reported in appendix (A).

2.3.8 du Pont/WFCCD

Observations were taken using the Wide Field reimaging CCD Camera (WFCCD) on the du Pont 100-inch telescope at Las Campanas Observatory using a 1 arcsec slit. The data were calibrated using HeNeAr arcs and bias subtraction, flat fielding and standard star observations for flux calibration. Reduction was performed with a modified version of PYDIS (Davenport, de Val-Borro & Wilkinson 2016) to extract and sky-subtract the spectrum.

For a journal of all the spectroscopic observations, see Table 1 and the complete sequence of spectra is shown in Fig. 1.

2.4 Optical photometric observations

2.4.1 Las Cumbres Sinistro

We observed AT2019dsg with the Las Cumbres Observatory Global Telescope Network (Brown et al. 2013). Observations were performed with the Sinistro cameras, mounted at the focus of 1-meter telescopes, at the following sites: South African Astronomical Observatory (CPT), Siding Spring Observatory (COJ), Cerro Tololo Interamerican Observatory (LSC), and McDonald Observatory (ELP). The target was observed with the Johnson B and V filters and the Sloan filters *g, r, i*. Data were reduced with the BANZAI pipeline (McCully et al. 2018), which performs standard data reduction routines such as bad-pixel masking, bias frames subtraction, dark subtraction, flat-field correction, and cosmic rays correction. The zero points of the images were calibrated using the American Association of Variable Star Observers (AAVSO) Photometric All-Sky Survey (APASS) DR10 (Henden 2019). The magnitudes were estimated with aperture photometry, using the IRAF task APPHOT, with a fixed aperture of 10 arcsec, to capture the light from the extended region of the galaxy.

2.4.2 LT IO:O

We observed AT 2019dsg using the Optical Wide Field camera (IO:O) at the Liverpool Telescope (LT) using the Sloan *g, r, i, z* and Johnson B and V filters. The images were reduced with the LT pipeline and the zero-points calculated using stars in the APASS catalogue. Magnitudes were estimated through aperture photometry (IRAF task APPHOT), using a fixed aperture of 10 arcsec.

2.5 Radio observations: e-MERLIN

We observed our target source, AT 2019dsg, with the e-MERLIN[3] radio interferometer in the UK between 2019 June 3 and September 12 (project code DD8006: PI Pérez-Torres). We observed AT 2019dsg a total of 13 times: 10 at C-band (4.82–5.33 GHz) and 3 at L-band (1.25–1.77 GHz). We summarize in Table 2 the start time of each observing run and its duration at each frequency band. All observations had a total bandwidth of 512 MHz divided in eight spectral windows of 64 MHz with 512 channels per spectral window, except runs 7 through 10, which had four spectral windows of 128 MHz each. We used 3C 286 and OQ208 as amplitude and bandpass calibrators, respectively. We correlated the phase calibrator, J2052+1619, at position $\alpha_{J2000.0} = 20^{h}52^{m}43\overset{s}{.}6199$ and $\delta_{J2000.0} = 16^{\circ}19'48\overset{''}{.}828$, which is separated 2.37 deg from our target, and we detected it clearly in all runs with a flux density of 0.32 and 0.42 Jy at C and L-band, respectively.

We carried out all reduction steps using the e-MERLIN CASA pipeline[4] version v1.1.16 running on CASA (McMullin et al. 2007) version 5.6.2. We followed the default procedures of the pipeline using the default parameters, but adding manual flag commands to remove bad data that the pipeline could not remove. We used a common model for the phase reference calibrator to calibrate and image each run. We then used the CASA task TCLEAN to image the target source, using the e-MERLIN CASA pipeline imaging procedure with Briggs weighting and a robust parameter of 0.5 for all runs except numbers 03 and 07, which required robust 0.0 and −1.0, respectively, due to the lack of the longest baselines. The cell size was 8 mas for the C-band data and and 20 mas for the L-band data. We show in Table 2 the synthesized beam size, local rms of the residual image, flux density, and luminosity of the target source measured as the peak of emission of a Gaussian fit to the deconvolved image.

3 ANALYSIS AND RESULTS

3.1 e-MERLIN observations

The source is an unresolved point-like source in all detected epochs, with no significant hints of extended emission. We computed the statistical astrometric uncertainty as the standard deviation of the positions of the centroid fitted to the images, resulting in a relative astrometric accuracy of about 6 mas (6.5 pc). We measured no

[2]https://github.com/svalenti/FLOYDS_pipeline

[3]http://www.e-merlin.ac.uk/

[4]https://github.com/e-merlin/eMERLINCASApipeline

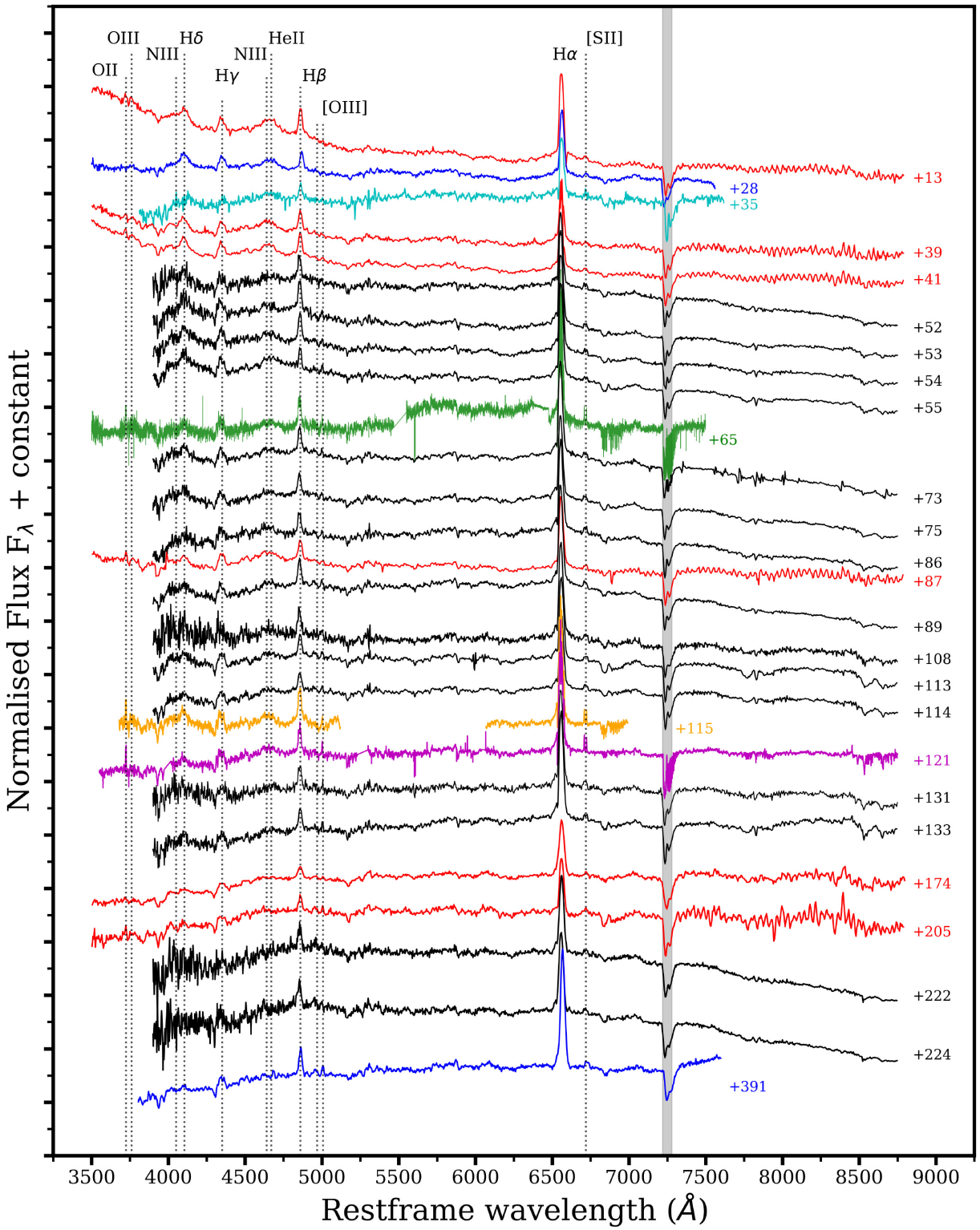

Figure 1. Sequence of spectra taken with EFOSC2 (red), DOLORES (blue), Du Pont (cyan), UVES (green), X-shooter (magenta), ISIS (orange), and with ACAM (black). For each spectrum, the phase with respect to the time of peak luminosity (MJD 58603.1) is reported on the right. The dotted lines indicate the main emission lines and the grey band represents the area affected by telluric absorption. The Hα line is affected by telluric absorption, but this is not shown in the plot for clarity. The UVES spectrum has been smoothed for clarity. All spectra have been corrected for foreground extinction. For plotting purposes, all spectra have been divided by their median value. The X-shooter, ISIS, and UVES spectra are not flux calibrated.

significant astrometric displacement from the C-band detections. The average position of AT 2019dsg is $\alpha_{J2000.0} = 20^{h}57^{m}02\overset{s}{.}9647$ and $\delta_{J2000.0} = 14°12'16\overset{''}{.}305$, as measured with respect to the phase reference correlation position quoted above. In L-band, we obtained 3σ upper limits on the flux density. We therefore combined the data from the three consecutive days of observations in the L-band and found a point-like source that is spatially coincident with the source in the C-band images. We obtain a 4σ detection of the source in

Table 2. Schedule of the e-MERLIN observations, with the run number, beam, and total flux density at each frequency band. Values of the non-detections are 3-σ level uncertainties with respect to the rms of the image. The last line is the 4.1σ detection from the combined L-band data.

Run	MJD (d)	Start date	Duration (h)	Frequency (GHz)	Beam_{maj} (mas)	$\text{Beam}_{\text{minor}}$ (mas)	Beam_{pa} (deg)	rms (μJy b^{-1})	Flux density (μJy)	Luminosity (10^{37}erg s^{-1})
01	58637.92	2019-06-03 22:00	12	5.1	67	32	28	32	160 ± 30	4.9 ± 0.9
02	58654.88	2019-06-20 21:02	12	5.1	71	32	28	21	340 ± 20	10.4 ± 0.6
03	58668.94	2019-07-04 22:32	10	5.1	764	580	76	86	410 ± 90	12.5 ± 2.7
04	58669.94	2019-07-05 22:32	10	5.1	96	29	28	24	460 ± 20	14.1 ± 0.6
05	58670.94	2019-07-06 22:32	10	5.1	98	30	27	23	490 ± 20	15.0 ± 0.6
06	58671.94	2019-07-07 22:32	10	5.1	99	29	27	23	480 ± 20	14.7 ± 0.6
07	58687.88	2019-07-23 21:17	10	5.1	177	54	14	128	680 ± 130	20.8 ± 4.0
08	58691.89	2019-07-27 21:22	9	5.1	92	30	20	42	650 ± 40	19.9 ± 1.2
09	58701.75	2019-08-06 18:00	11	5.1	69	33	25	27	770 ± 30	23.6 ± 0.9
10	58738.68	2019-09-12 16:13	11	5.1	78	29	28	31	1210 ± 30	37.0 ± 0.9
11	58688.88	2019-07-24 21:17	10	1.5	293	119	22	40	<120	<1.1
12	58689.91	2019-07-25 21:50	9	1.5	322	115	21	44	<130	<1.2
13	58690.89	2019-07-26 21:20	9	1.5	285	108	23	38	<115	<1.0
				1.5					145 ± 35	1.3 ± 0.3

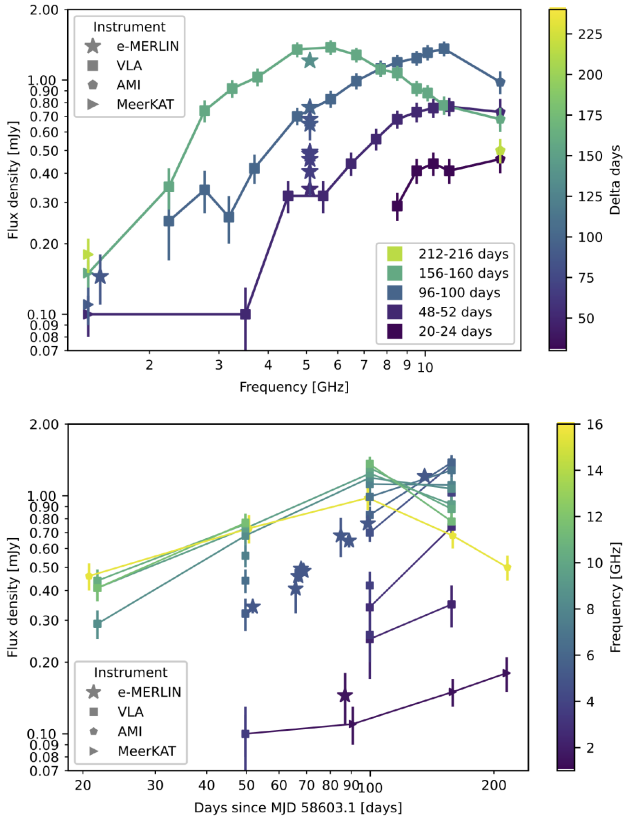

Figure 2. Radio evolution of AT 2019dsg. VLA, AMI, and MeerKAT data are from Stein et al. (2020), while e-MERLIN data (stars) are our own data. The e-MERLIN data are not connected by solid lines for readability. Note the characteristic synchrotron shift of the peak frequency with time, so by day ∼160 the radio emission at frequencies above ∼6.0 GHz is already in its optically thin, decaying phase, while at smaller frequencies is still in its optically thick, increasing phase.

the L-band with a flux density of 145 ± 35 μJy, corresponding to a luminosity of $1.3 \pm 0.3 \times 10^{37}$ erg s^{-1} .

We show in Fig. 2 the radio light curve of AT 2019dsg for the first ∼200 d at multiple frequencies, including our e-MERLIN data. The e-MERLIN interferometer provides a better angular resolution than any of the other instruments. Therefore, the observed flux is not contaminated by background emission, so our observations provide bona fide flux densities against which to test the baseline of radio emission assumed in Stein et al. (2020). Overall, it appears that the agreement is good.

3.2 Host velocity dispersion measurement

We use the X-shooter spectrum to constrain the width of the host galaxy absorption lines. In particular, we use the penalized pixel fitting routine PPXF (Cappellari 2017) to perform full spectrum template fitting with the Elodie stellar template library (Prugniel & Soubiran 2001). We resample the X-shooter spectrum within the errors and measure velocity dispersions for 1000 realizations of the data (see Wevers et al. 2017 for a detailed explanation of the method). Fitting the resulting velocity dispersion distribution with a Gaussian model, we find a mean FWHM of 94 km s^{-1} with a standard deviation of 1 km s^{-1}, which we adopt as the velocity dispersion and its measurement uncertainty. Using the M–σ relation of Gültekin et al. (2009) and adding the measurement errors linearly with the scatter in the relation, this corresponds to a black-hole mass of $\log(M_{BH}) = 6.73 \pm 0.40$ M$_\odot$. We note that by using both the M-sigma relations of Ferrarese & Ford (2005) and of McConnell & Ma (2013), we obtain a value for the black-hole mass which is compatible with the previous estimate within uncertainties. This corresponds to an Eddington luminosity $L_{\text{Edd}} = (6.8 \pm 4.1) \times 10^{44}$ erg s^{-1} and a Schwarzschild radius of $R_S = (1.6 \pm 0.9) \times 10^{13}$ cm, for a non-rotating BH.

3.3 UV/optical light curve

The host galaxy is marginally detected in the GALEX NUV band (λ_{cen} = 2328 Å; NUV = 21.1 ± 0.4), indicating that even in the latest epochs (+180 d), when the source was detected at a magnitude of UVM2 (λ_{cen} = 2260 Å) = 18.95, host contamination is not an issue in the UV bands. To check the host galaxy contamination in the optical, we use the Kron magnitudes from Pan-STARSS (PS) Data Release 2, using the filter transformations from Jordi, Grebel & Ammon (2006), when necessary.

In the optical, the transient is detected above the host galaxy light in the U, B, V, *g*, and *r* bands, until ∼140 d after peak. We remove the host galaxy contribution by subtracting the flux derived from the Kron magnitudes from PS. We plot the host-subtracted UV/optical light curve in Fig. 3, where we report also the *g* and *r* data from van Velzen et al. (2020). The host-subtracted magnitudes are reported in Table C1.

3.3.1 UV/optical BB fitting

Since our additional photometric observations are consistent with that already presented in the literature, and do not cover a significantly longer time after peak light, we do not create an SED for the source, but we use the results from van Velzen et al. (2020) and Stein et al. (2020). They find that the UV/optical light curve is well fit by a black body (BB) with roughly constant temperature $T = (3.9 \pm 0.2) \times 10^4$ K and radius $R = (3.9 \pm 0.3) \times 10^{14}$ cm. The observed peak bolometric luminosity is $L_{bb} = (2.9 \pm 0.3) \times 10^{44}$ erg s^{-1} $\sim 0.4 L_{Edd}$.

3.4 X-ray spectral analysis

3.4.1 Swift/XRT

To fit the Swift X-ray spectrum, we use XSPEC 12.10.0 (Arnaud 1996) in HEASOFT v6.24, and assume a Galactic column density of $n_H = 6.45 \times 10^{20}$ cm^{-2} (HI4PI Collaboration 2016). Due to the low number of counts in each bin, we use Cash statistics (the results are identical when rebinning the spectrum to 20 counts/bin and using Gaussian statistics). Confidence intervals are quoted at the 90 per cent level (ΔC-stat = 2.71). A 65 ± 6 eV BB model (TBabs × zashift × bbodyrad) provides a good fit to the data (cstat = 137 for 682 dof or $\chi^2 = 0.81$ with 9 dof), with a radius $R = 3.4^{+1.5}_{-0.9} \times 10^{11}$ cm. Using instead a multitemperature BB model (discbb) yields kT = 80 ± 7 eV (cstat = 135 for 682 dof). These results are in agreement with those presented in Stein et al. (2020). To convert the count rates to unabsorbed 0.3–10 keV fluxes, we assume the simple BB model with Galactic extinction, which gives a conversion factor of 9.1×10^{-11} cts/erg/cm^2/s.

3.4.2 NICER

Background-subtracted NICER spectra are fit to the same absorbed, redshifted BB model used for the Swift/XRT spectrum. The source is not detected over the NICER background above 1 keV, and fits are conducted in the 0.3–1 keV bandpass, with luminosities and count rates referring to this energy range. The latest effective area (*nixtiaveonaxis20170601v004.arf*) and response matrix (*nixtiref20170601v002.rmf*) files are utilized. The BB temperature for the late-time spectrum is fixed at 30 eV. The results are shown in Table 3, and are consistent with the analysis of the Swift/XRT spectrum.

The 0.3–10 keV X-ray light curve is shown in Fig. 4, where we have used the webPIMMS[5] tool to convert the NICER 0.3–1 keV luminosities to the 0.3–10 keV energy range for consistency with the XRT data. The X-ray luminosity shows a rapid decay from 3×10^{43} erg s^{-1} to 10^{42} erg s^{-1} over 25 d. Then, the decay becomes more shallow and the X-ray luminosity reaches 3.6×10^{41} erg s^{-1} in the last epoch at which the source is detected (∼100 d after peak). The XRT light curve shows variability of factor 2–3 on a time-scale of days during the initial rapid decrease, while this behaviour is not seen in the NICER data. In Fig. 5, we plot the evolution of the BB temperature with time. The temperature decreases from 70 to 40 eV over ∼15 d. In Fig. 6, we plot the 0.3–1 keV X-ray luminosity versus the BB temperature from the fit to the NICER data. We overplot the data with a $L_X \propto T^4$ curve.

3.5 Optical spectroscopy

The sequence of spectra from EFOSC2, DOLORES, UVES, X-shooter, ISIS, and ACAM is shown in Fig. 1. The first spectra show a blue continuum that decays over time. The decay of the blue part of the spectrum pivots around 5000 Å. The continuum is dominated by the host galaxy redwards of this wavelength at all stages of the TDE outburst. After roughly 40 d, the blue continuum light has decayed. Coincidentally, this is similar to the time-scale over which the X-ray rapidly decays. The spectra show strong Balmer emission lines (Hα through Hδ) and a broad He II emission line that becomes less visible with respect to the surrounding continuum over time. We also identify the O II doublet at 3726 and 3729 Å and O III at 3760 Å in emission.

3.5.1 Subtraction of the stellar component

The spectra clearly show absorption features due to the host galaxy, more prominently in the medium-high resolution spectra. To remove the stellar contribution, we employ PPXF: we build a synthetic host galaxy spectrum by fitting stellar spectra to our X-shooter spectrum. The method convolves a series of stellar template spectra to the observed spectrum (host galaxy+TDE), by combining the individual stellar templates with additive and/or multiplicative orthogonal polynomials and an initial guess of the line-of-sight velocity dispersion. The best-fitting template (or combination of templates) is then found by χ^2 minimization. The emission features and areas affected by telluric absorption are masked during the template convolution procedure. This method therefore removes from the observed spectra the stellar component from the host galaxy. We employ the PHOENIX high resolution synthetic spectral library[6] (Husser et al. 2013); this library covers the whole wavelength range of the UVB and VIS arms of X-shooter (3000–10 000 Å) with a resolution of R∼50 000. Of the whole library, which contains ∼30 000 synthetic spectra covering a broad range of stellar properties, we select a subsample with effective temperature 2300 K $\leq T_{eff} \leq$ 12 000 K, metallicity in range $-2.0 \leq$[Fe/H]≤ 1.0 and alpha elements abundance [α/Fe] = 0. This library does not contain emission line templates. We use the X-shooter spectrum as a basis for building our synthetic host galaxy spectrum as it is the highest resolution spectrum on which we can apply the PPXF routine: the ISIS spectrum does not have enough continuum free from emission features and the continuum of the UVES spectrum has too low a SNR to make the routine converge. We then use again the PPXF code to scale the synthetic host spectrum to the other spectra of our follow-up. Since this is not possible for spectra with a higher resolution, we did not perform the subtraction on the UVES spectrum. After the subtraction, the continuum of the spectra is scaled to 1, using the median of the flux.

The host subtracted spectra (shown in Fig. 7) still show strong Hα and Hβ emission lines, both with a broad (FWHM∼5000–10 000 km s^{-1}) component at the base, and a narrower (FWHM∼1000 km s^{-1}) peak. Due to the redshift of the host galaxy,

[5] https://heasarc.gsfc.nasa.gov/cgi-bin/Tools/w3pimms/w3pimms.pl

[6] http://phoenix.astro.physik.uni-goettingen.de/

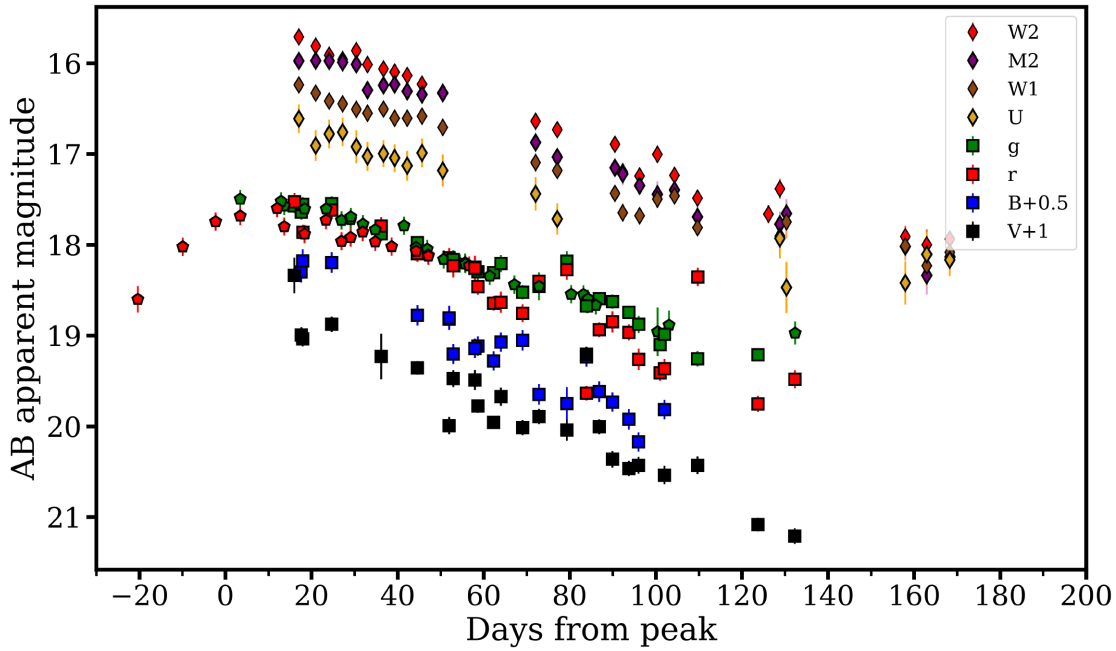

Figure 3. Host-subtracted, extinction corrected light curve of AT 2019dsg, in AB magnitudes: UVW2 (red diamonds), UVM2 (purple diamonds), UVW1 (brown diamonds), U (orange diamonds), *g* (green squares and pentagons), *r* (red squares and pentagons), B (blue squares), and V (black squares). The pentagons indicate the ZTF data from van Velzen et al. 2020.

Table 3. Best-fitting model parameters derived from time-resolved *NICER* X-ray (0.3–1 keV) spectra. The temperature in the last epoch is kept fixed at 30 eV and the luminosity value is a 3σ upper limit.

ObsIDs	0.3–1 keV count rate (cts s^{-1})	Average time (MJD)	Exposure (seconds)	kT (eV)	c-statistic	Degrees of freedom	Luminosity (10^{42} erg s^{-1})
200680102	2.02	58625.8	2159	68 ± 1	82.19	67	$32.5^{+1.0}_{-0.9}$
200680103-4	1.71	58630.3	767	67 ± 2	46.54	67	$28.1^{+1.6}_{-1.5}$
200680105	1.48	58633.16	593	65 ± 3	75.54	67	$25.0^{+2.0}_{-1.7}$
200680106	1.09	58634.06	627	63 ± 3	58.86	67	$18.9^{+1.5}_{-1.4}$
200680107-8	0.4	58639.21	239	43^{+8}_{-7}	55.26	67	$9.8^{+2.5}_{-2.11}$
200680110-12	0.02	58759.99	15493	30	108.7	68	<0.63

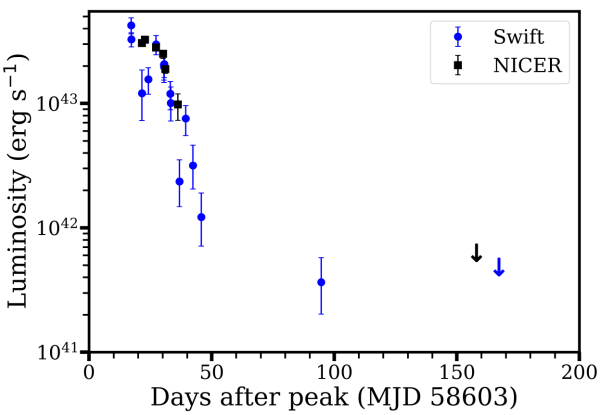

Figure 4. The 0.3–10 keV X-ray luminosity evolution with time of AT 2019dsg. In blue (circles for detections), the Swift data, in black (squares for detections), the NICER data. The downward arrows represent 3σ upper limits.

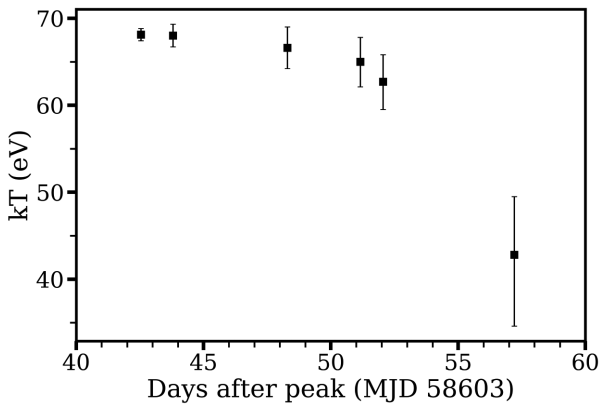

Figure 5. Evolution of the BB temperature from the fit to the NICER (0.3–1 keV) data with time.

the Hα line is contaminated by the telluric absorption band at ~6900 Å. This is most clearly visible in the ISIS, UVES, and X-shooter spectra, due to the higher resolution of these spectra. Redwards of Hα, the two [S II] lines (6716 and 6731 Å) are visible and resolved in some spectra. The Hγ, Hδ, and the broad He II lines are still detected and the [O III] doublet (4959, 5007 Å) becomes clearly visible. Also

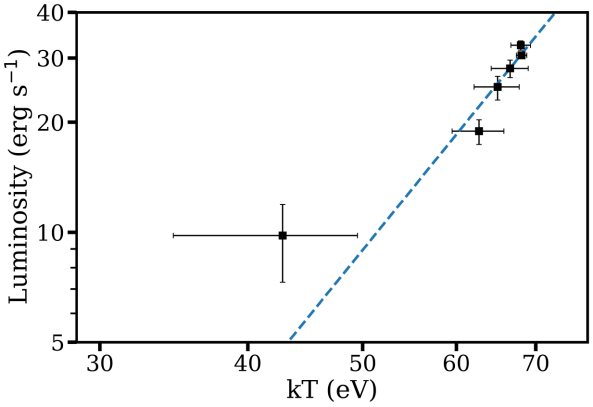

Figure 6. X-ray luminosity (0.3–1 keV) versus the BB temperature. The dashed line represents L $\propto$ kT^4 with arbitrary normalization. The observed rate of cooling decreases over time.

the O II doublet (3726, 3729 Å) and a weak O III at 3760 Å are still detected. We fit the emission lines of the host subtracted spectra with multiple Gaussian components, combined with a polynomial to fit the local continuum, using PYTHON code employing the LMFIT[7] package (Newville et al. 2014). During the fitting procedure, we tied the FWHM and the separation of the [S II] lines and of the [O III] lines, when the doublets were resolved. The central wavelengths of the broad base and the narrow peak of Hβ are also tied together, to reduce the number of free parameters in this region. We were not able to fit the [N II] doublet at 6548 and 6583 Å, probably due to the presence of the telluric absorption. Example Hα and Hβ line fits are shown in Figs 8 and 9, respectively.

After the subtraction procedure, from the spectrum of 2019 September 09 (133 d after peak) onward, the broad bases of Hα and Hβ are not detected anymore. The He II line is not detected after the spectrum of 2019 November 21 (205 d after peak). We therefore associate these lines with the transient event, while we consider the remaining, more narrow, emission features as due to star formation in the host galaxy instead (see Section 4.1). At late times (more than 200 d after peak), in the continuum between Hβ and Hα, metal lines appear. In Fig. 10, we show a comparison between AT 2019dsg and two other TDEs that have shown metal lines in the same wavelength range during their evolution: ASASSN-15oi and AT2018fyk (Wevers et al. 2019b). In the spectrum of AT 2019dsg, we can clearly identify absorption lines from Na I and Mg Ib and many emission lines from Fe II, as well as the Fe II absorption feature at 5264 Å.

We took a late time spectrum with TNG on 2020 May 24 (391 d after peak, last spectrum of Figs 1 and 7), after the object came back from behind the Sun. In this spectrum, we clearly see the narrow Hα and Hβ, [O III] and [S II] lines, a still strong Hγ and weak Hδ emission lines. The aforementioned metal lines are not present in this spectrum.

3.5.2 *X-shooter, ISIS, and absorption lines*

The Hβ region of the X-shooter spectrum is plotted in Fig. 11. The spectrum shows the [O III] doublet (4959 and 5007 Å), the Hβ line with the usual two components, the broad He II, and the Hγ line. The Hγ emission line shows an absorption line superimposed and the He II shows two absorption features.

[7]https://lmfit.github.io/lmfit-py/

The host subtracted ISIS spectrum shows a similar morphology, albeit the absorption features in the He II line are less pronounced. The fit to the Hγ and He II emission lines of the ISIS spectrum is shown in Fig. 12. The absorption lines on top of the Hγ and He II emission lines are present in both the original spectrum, before the subtraction of the host galaxy light, and in the host-subtracted one. The FWHM, equivalent width (EW) and central wavelength of these absorption lines are reported in Table 4. The absorption line parameters are within uncertainties between the two spectra.

The resolution in the spectra obtained during the remainder of our follow-up campaign is not high enough to investigate these absorption features in detail (we will discuss the UVES spectrum separately in Section 3.5.4). In both the ISIS and X-shooter spectra, the Hα line is strongly affected by the atmospheric absorption that we were not able to correct completely with MOLECFIT (see Section 2.3.5), therefore a precise fit of the Hα line was not possible. None the less, in the host-subtracted spectra, the two [S II] lines (6716 and 6731 Å) are clearly detected and resolved. In the lower resolution spectra of our follow-up campaign, the two lines often blend together.

3.5.3 *Line-fitting results*

We report the results of the line fitting in Tables B1, B2, and B3. We plot the evolution of the line parameters resulting from the fit: the FWHM, EW, and shift with respect to the rest frame wavelength are shown in Figs 13, 14, and 15, respectively.

The values of the FWHM have been corrected for the instrumental broadening, measured from the sky lines of the spectra. The FWHM (Fig. 13) of the broad components of Hα and Hβ have different values but a similar evolution. The FWHM of the broad Hα starts at 12 000 km s^{-1}, decreases to almost 5000 km s^{-1} over 30 d and then increases to the initial value of 12 000 km s^{-1} in $\sim$20 d, to stay at this value until it is no longer detected, 130 d after peak. The FWHM of the broad Hβ has an initial value around 5000 km s^{-1}, and for the whole duration of the follow-up campaign fluctuates between 4000 and 8000 km s^{-1}. There are some significant outliers that could be due to the corresponding spectra having a low SNR, while others could be caused by variations due to uncertainties in the subtraction process. The initial evolution of the FWHM of Hγ is similar to the one observed for the broad Hα (albeit with lower values): it starts at 3500 km s^{-1}, to then decreases to 2000 km s^{-1}over 30 d. It then remains around this value until the end of our follow-up campaign. The Hδ line in all the ACAM spectra is not well constrained, because it falls at the edge of the wavelength range covered. Therefore we do not fit it at these epochs. Its FWHM has an initial value similar to the one of Hγ at 4000 km s^{-1}, it then increases to 4500 km s^{-1} at the next epoch (20 d later), to then gradually decrease to 3000 km s^{-1}between phase 40 and 90. The FWHM of He II goes from 10 000 to 5500 km s^{-1}in the first 30 d, then increases up to 10 000 km s^{-1} in 30 d, to then decrease to 7000 km s^{-1} between 60 and 140 d. In the last two epochs, the FWHM of He II increases up to 13 000 km s^{-1}. The time-scale of the initial decay of the FWHM of the broad Hα, Hβ, and the He II is similar to the time-scale of the decay of the X-ray light and of the blue continuum. Finally, the FWHMs of the narrow peaks of Hα and Hβ do not show evolution over the time of observation and vary around 1000 km s^{-1}, except for two outliers at 175 and 205 d after peak, when the narrow Hβ has a FWHM above 1500 km s^{-1}. These points are due to the low SNR of the corresponding spectra. The values of the FWHM of the narrow

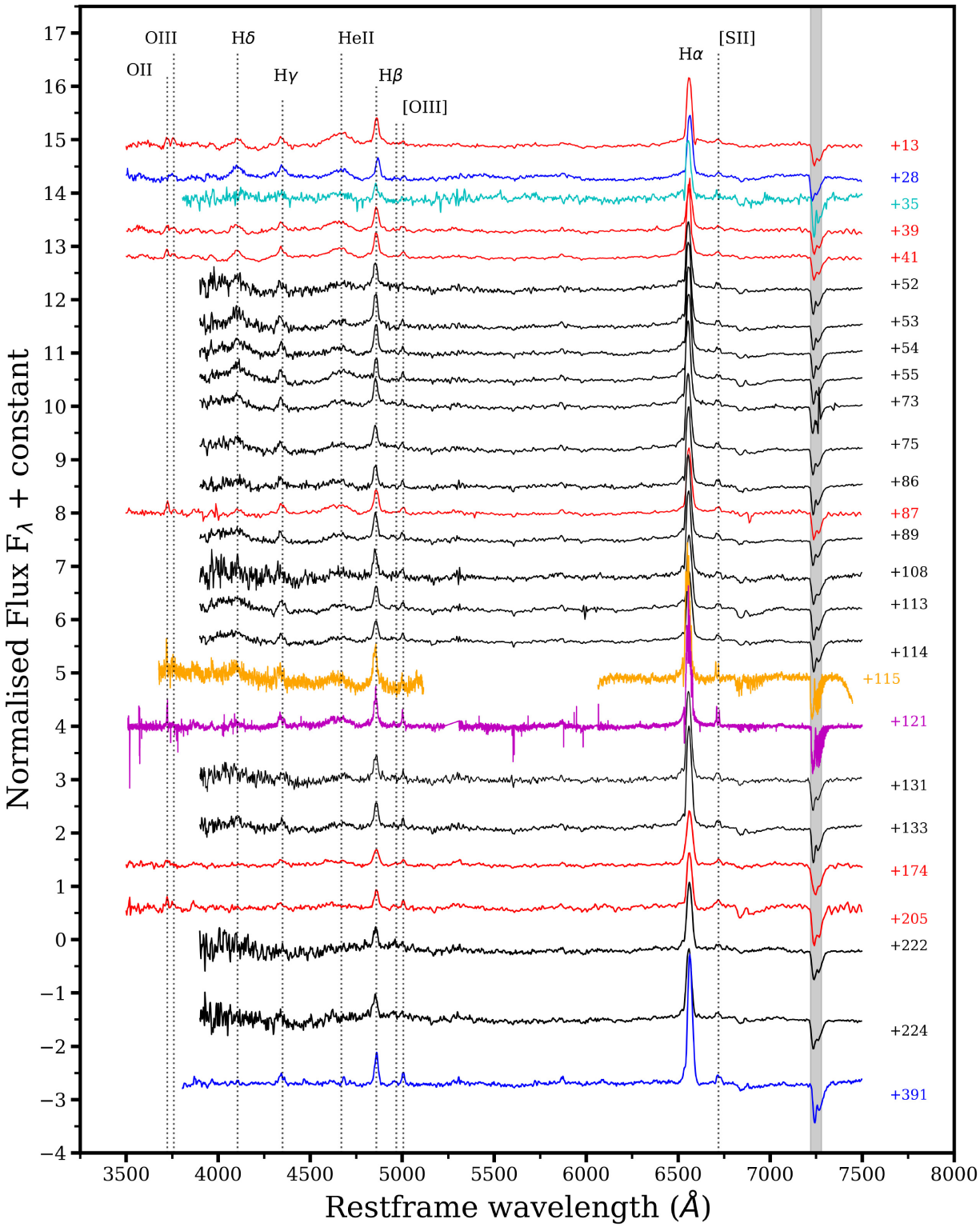

Figure 7. Sequence of host-subtracted spectra taken with EFOSC2 (red), DOLORES (blue), Du Pont (cyan), X-shooter (magenta), ISIS (orange), and with ACAM (black). For each spectrum, we annotate to the right the number of days passed since the time of peak luminosity (MJD 58 603.1). The dotted lines indicate the main emission lines and the grey band represents the area affected by telluric absorption. The Hα line is affected by telluric absorption, but this is not shown in the plot for clarity. All spectra have been corrected for foreground extinction. For plotting purposes, all spectra have been normalized. The X-shooter and ISIS spectra are not flux calibrated.

Hα and Hβ peaks obtained from the late-time spectrum (+391 d) are both around 1200 km s^{-1}.

In Fig. 14, we plot the evolution of the EW of the emission lines with time. The EW of the broad base of Hα decreases from an initial

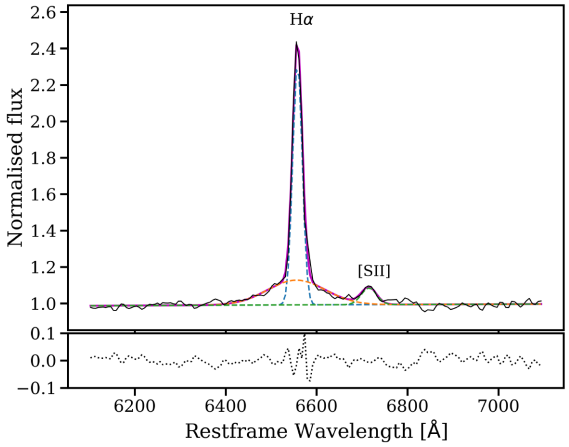

Figure 8. Example of the fit to the Hα and [S II] emission lines in the EFOSC2 spectrum taken on 2019 June 10 (41 d after peak), after performing the host galaxy subtraction. The dashed lines represent different Gaussian components, while the solid line represents the total fitting function. The residuals of the fit are shown in the bottom panel.

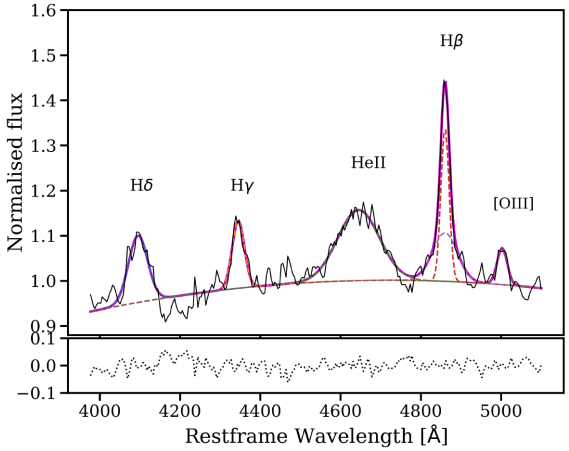

Figure 9. Example of the fit to the emission lines in the Hβ region of the EFOSC2 spectrum taken on 2019 June 08 (39 d after peak), after the subtraction of the stellar component process. The dashed lines represent different Gaussian components, while the solid line represents the total fitting function. The residuals of the fit are shown in the bottom panel.

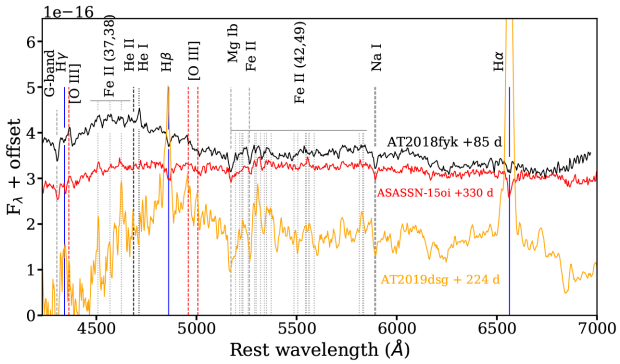

Figure 10. Comparison between the spectra of AT 2019dsg (orange) at +224 d and AT2018fyk (black) at +85 d and ASASSN 15oi (red) at +330 d, the other two TDES that have shown Fe lines in their optical spectra.

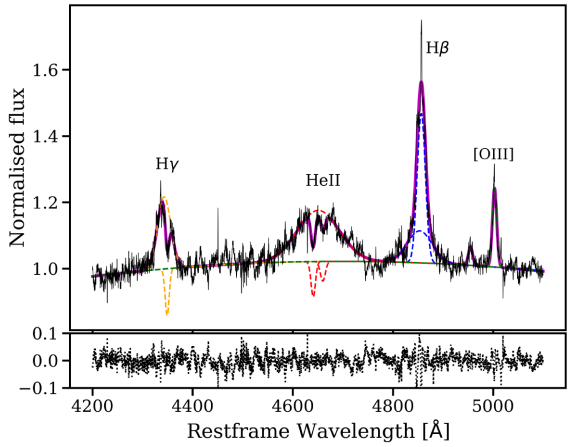

Figure 11. Fit to the emission lines in the Hβ region of the host galaxy subtracted X-shooter spectrum obtained 121 d after peak light. The dashed lines represent different Gaussian components, while the solid line represents the total fitting function. The residuals of the fit are shown in the bottom panel.

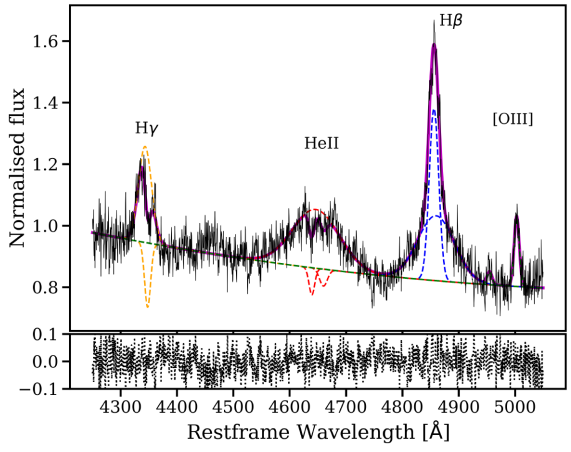

Figure 12. Fit to the emission lines in the Hβ region of the host galaxy subtracted ISIS spectrum obtained 115 d after peak light. The dashed lines represent different Gaussian components, while the solid line represents the total fitting function. The residuals of the fit are shown in the bottom panel.

Table 4. Hγ and He II absorption lines.

	H$_\gamma$	He II	He II
FWHM$_I$	829 ± 128	656 ± 140	983 ± 317
FWHM$_X$	649 ± 39	1065 ± 50	757 ± 42
EW$_I$	−2.6 ± 0.6	−1.1 ± 0.3	−1.0 ± 0.4
EW$_X$	−1.4 ± 0.1	−2.5 ± 0.2	−1.4 ± 0.1
WL$_I$	4348.3 ± 0.6	4639.2 ± 0.8	4658.8 ± 1.6
WL$_X$	4349.1 ± 0.2	4641.9 ± 0.3	4662.1 ± 0.3

FWHM (in km s^{-1}), EW (in Å), and central wavelength (WL, in Å) of the absorption lines superimposed the Hγ and He II emission lines in the X-shooter and ISIS spectra (Figs 11 and 12, respectively). With I, we indicate the results from the fit to the ISIS spectrum (+115 d) and with X, the ones from the X-shooter spectrum (+121 d). The values have been corrected for the instrumental broadening.

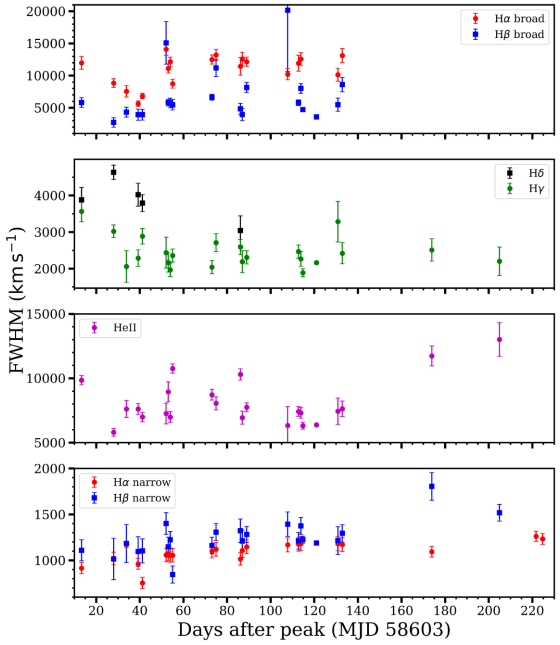

Figure 13. Evolution of the FWHM of the emission lines. In the first panel, the broad base of Hα (red circles) and Hβ (blue squares); in the second panel, Hγ (green circles) and Hδ (black squares); third panel, He II (magenta circles). These three lines are due to the TDE. In the bottom panel, the narrow peaks of Hα (red circles) and Hβ (blue squares) are shown, these lines are due to host galaxy activity. On the *x*-axis, the number of days passed since the light-curve peak is reported.

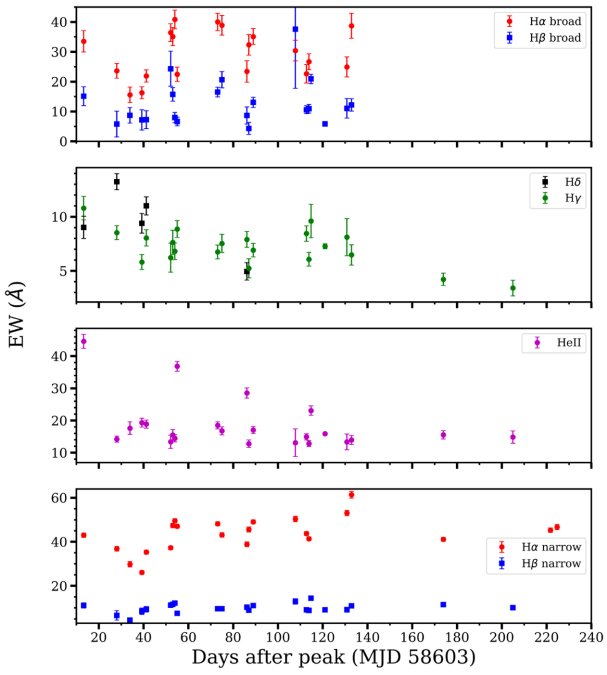

Figure 14. Evolution of the EW of the emission lines. From top to bottom: the broad Hα (red circles) and Hβ (blue squares), the Hδ (black squares) and the Hγ (green circles), and the He II (magenta circles) emission lines caused by the TDE. Bottom panel: the narrow Hα (red circles) and Hβ (blue squares) emission lines originating in the host galaxy. Note that the redshift of AT 2019dsg caused the Hα region to coincide in wavelength with the prominent telluric feature, rendering the derived EW of Hα uncertain. The number of days passed since the light curve peak is given on the *x*-axis.

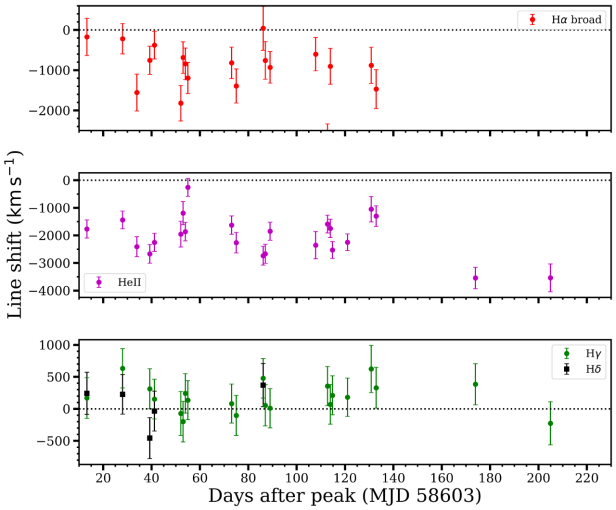

Figure 15. Evolution of the shift with respect to the laboratory central wavelength of the emission lines. From top to bottom: the broad Hα (red circles), the He II (magenta circles), the Hδ (black squares), and Hγ (green circles) emission lines caused by the TDE. The central wavelength of the broad Hβ component was fixed during the fitting process and is not shown (see text). The number of days passed since the light curve peak is given on the horizontal axis. Negative values indicate a blue-shift with respect to the rest frame wavelength.

value of 35–20 Å in 30 d, then increases to 40 Å at phase +60, to then decrease again to 25 Å over the rest of the follow-up campaign, except for the last epoch, when the EW is at 35 Å. The EW of the broad base of Hβ varies between 5 and 20 Å, to then stabilize around 10 Å in the last ∼40 d. The higher values are also in this case due to low SNR and uncertainties during the subtraction process, rather than being indicative of variability in the line. The EW of the Hγ line starts at 10 Å, to then decrease to 5 Å after 30 d. It subsequently remains constant until the last two epochs in which the EW is 4 Å. The Hδ line follows a very similar evolution, except for the value at 30 d after peak. The EW of the He II has an initial value of 40 Å and, already 20 d after this (30 d after peak), it decreases to 10 Å, where it remains almost constant for the next 100 d. The outliers at 80 and 110 d, with an EW above 30 Å, are possibly due to uncertainties in the subtraction process. The initial evolution matches the time-scale of the decay of the blue continuum of the TDE. Finally, the EW of the narrow Hβ remains constant around 10 Å, while the EW of the narrow Hα varies around 40 Å. The small scale variations of the Hα narrow peak are likely due to variations of the telluric absorption.

We plot the shift with respect to the restframe wavelength of the emission lines in Fig. 15 (we indicate blue shifts with negative values). To reduce the number of free parameters, during the fitting procedure, the central wavelength of the broad Hβ was tied to the one of the narrow peak, which, due to the high SNR in that line, dominates the fit result of this parameter (we do not show the shift of the broad Hβ in the plot). The broad Hα shows a blue shift that fluctuates between 0 and −2000 km s^{-1}, without a clear evolution with time. The He II line is blueshifted by −2000 km s^{-1} at the first epoch of observation. The value of the shift fluctuates around this value for the first ∼130 d (except one outlier at 55 d), then decreases to −1000 km s^{-1} at 130 d. In the last two epochs at which the line is detected, the blue shift has increased to −4000 km s^{-1}. The shift of the Hγ and Hδ line is always below |500| km s^{-1} and is constant within uncertainties. It is worth noting that the velocity offsets can be

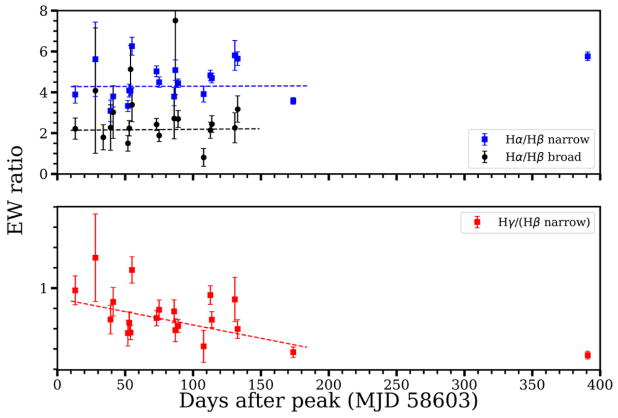

Figure 16. Ratio of the EW of Balmer lines. Top panel: narrow Hα/Hβ in blue squares and broad Hα/Hβ in black squares, both fitted with a straight line. The changes in the ratio between the narrow peaks are due to changes in the telluric absorption. Bottom panel: the ratio of the EW of the Hγ and the narrow Hβ emission line. On the x-axis, the number of days since the light curve peak is reported.

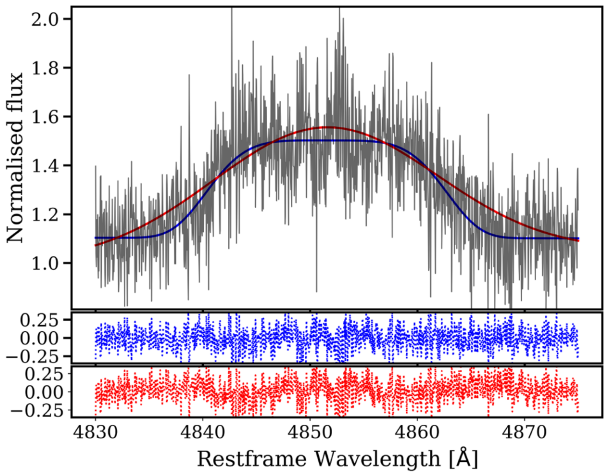

Figure 17. Hβ region of the UVES spectrum with two different fits: in red, the fit with a Gaussian curve, similar to the function used in the other spectra and in blue, the fit using a flat-top Gaussian. The two bottom panels are the residuals of the two fit, the top one for the flat-top Gaussian fit and the bottom one for the Gaussian fit.

affected by O(10^2) km s^{-1} due to good observing conditions: when the seeing is better than the slit width, due to potential non perfect centering of the source in the slit, such changes can be induced. The narrow peaks of Hα and Hβ are always shifted by less than |500| km s^{-1} and are not plotted. The shift of Hα and Hβ at each epoch is not of the same value. If we assume that the narrow Hα and Hβ originate from the host galaxy, we can expect their central wavelength to be at the laboratory values. We can use the shift measured in their central wavelength as a proxy for wavelength calibration issues or for aforementioned uncertainties due to the observing conditions. We therefore use the values of the shift calculated for the narrow peak of Hα and Hβ to estimate an additional uncertainty that is reflected in the error bars of Fig. 15.

We plot the flux ratio of the Balmer lines in Fig. 16 and we fit the data with a straight line. The ratio of the narrow peaks of Hα and Hβ shows a slight increase over time. During the first ∼200 d of observations, it remains almost constant at an average value of 4.5, to then increase to 5.8. The reduced χ^2 of the fit is bad, with a value of 6.4. The ratio of the broad bases of Hα and Hβ remains constant within uncertainties at an average value of 2.4 (reduced χ^2= 1.9). The ratio between Hγ and the narrow peak of Hβ decreases from 1 to 0.3, which is also the value at the last epoch. The fit with a straight line to the data of the first ∼200 d of observations has a reduced χ^2 of 1.8.

3.5.4 UVES spectrum

It is interesting to consider the UVES spectrum by itself, given its higher resolution. In Fig. 17, we show the Hβ region of the spectrum (Hα is strongly affected by the telluric absorption, while the other emission lines are not strong enough with respect to the continuum, which is very noisy). The emission line in the UVES spectrum has a more box-like shape, instead of the Gaussian shape used to fit for lower resolution spectra. The line also shows evidence for structure on top. We fit this line both with a single Gaussian curve (in red in the plot), mimicking the fit of the other spectra, and with a 'generalized' Gaussian (in blue): $f(x) = a \cdot exp[-\left(\frac{x-c}{2\sigma}\right)^n]$ with n > 2 to get a flat top (n ≃ 5 from our fit). While the errors on the spectrum are too large to compare the reduced χ^2 and assess the goodness of fit, visually the flat-top Gaussian describes the wings of the line better. On top of this, looking at the residuals, we can see that in the case of the 'regular' Gaussian fit (bottom panel of Fig. 17, in red) there are small trends in the wings of the line (4840–45 and 4862–68 Å), with respect to the flat-top Gaussian fit.

The difference between the shape of the Hβ line in the UVES spectrum and in the other spectra can be accounted for by considering the different resolution. We rebin this spectrum, artificially lowering the resolution, to match the ACAM spectrum taken on 2019 July 11, which is the closest in time. The resulting spectrum is visually very similar to the ACAM one. We then fit the rebinned UVES spectrum with the line structure used for the other spectra (of which an example is shown in Fig. 9) and we obtain line parameters within uncertainties of the ones derived from the July 11 ACAM spectrum. Notably, the broad base of Hβ and the He II were difficult to constrain on the unbinned UVES spectrum, probably due to the low SNR in the continuum. The complex structure at the top of the emission line is consistent with that seen in the X-shooter (Fig. 11) and ISIS spectra.

4 DISCUSSION

Before discussing the interpretation of the results of our observations and analysis, we summarize the main results.

The transient is bright in X-rays, UV, optical, and radio. The X-ray light curve decays very quickly and the transient becomes undetected ∼100 d after peak, while the low-frequency radio luminosity is seen to be increasing steadily. The optical spectra show a blue continuum that decays over the first 40 d of our observations. In addition, multiple broad emission lines are detected. After subtracting the stellar component of the host galaxy light, the spectra show Balmer (Hα through Hδ) and He II 4686 Å emission lines. The [O III] and [S II] doublets (4959, 5007 and 6716, 6731 Å, respectively) are also detected in emission. The Hα and Hβ emission lines show two components: a narrow peak and a broad base. We consider the broad base of Hα and Hβ, as well as the He II line to originate from the TDE, while the narrow emission lines as due to emission from the host galaxy. However, we do consider the narrow Fe II emission lines appearing ∼200 d after peak in the optical spectra to be caused by the TDE. In a late time host galaxy spectrum, the broad bases of Hα and Hβ, the He II and the Fe II lines are no longer detected. Our

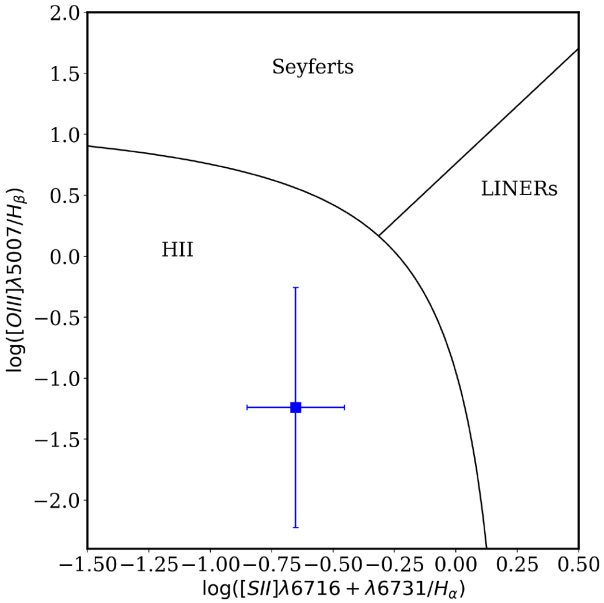

Figure 18. Position of the persistent narrow emission lines in the host galaxy spectrum of AT 2019dsg on a BPT diagram. The spectrum used was the late time TNG spectrum at 391 d, when no broad components to the Balmer lines could be detected. The lines separating the different regions come from Kewley et al. (2001).

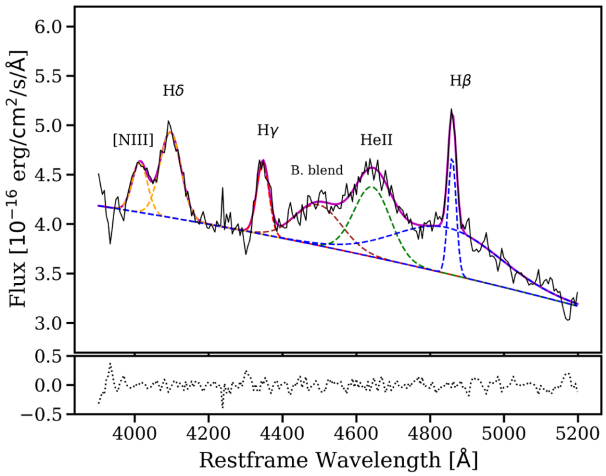

Figure 19. Example of a fit to the emission lines in the Hβ region of the EFOSC2 spectrum taken on 2019 June 08 (+39 d), before performing the host galaxy subtraction. With "B. blend" we indicate a spectral feature that, in previous works, was associated with a blend of unresolved lines due to the Bowen fluorescence mechanism. In the bottom panel, the residuals of the fit are shown.

medium/high resolution spectra show absorption lines superimposed on some emission lines and some emission lines show a deviation from a Gaussian profile.

4.1 Constraints on the presence of an AGN

The persistence of the Balmer lines in our late time spectra, especially the narrow Hα and Hβ peaks, the small offset and FWHM of these lines, coupled with the apparent absence of line evolution, indicate that those narrow emission lines do not originate in the transient event, but rather in a weak active galactic nucleus (AGN) or are caused by star-forming activity. In order to assess the underlying ionizing mechanism for these narrow emission lines, we plot the position of the source on a Baldwin, Phillips & Terlevich (BPT) diagram (Baldwin, Phillips & Terlevich 1981) in Fig. 18. Due to the presence of the telluric absorption on top of the Hα and [N II] doublet lines, we were not able to constrain the presence of the latter. Therefore, we are limited in the number of BPT diagrams we can use. For the BPT diagram, we use the values of the line parameters calculated from the last spectrum available, 391 d after peak. The source falls in the H II region of the diagram, indicating that star formation is responsible for these narrow emission lines. In addition, the mid-infrared colour from the Wide-field Infrared Survey Explorer, at W1–W2 = −0.05, is lower than the threshold presented in Stern et al. (2012) for AGNs, also suggesting that the SMBH was not active prior to the TDE.

van Velzen et al. (2020) mention that the host galaxy falls in the green valley when plotting the intrinsic u−r colour versus the host galaxy mass, a region that also hosts post-starburst galaxies. The narrow Hα and Hβ lines have a FWHM above 1000 km s^{-1}, which is higher than expected from an AGN narrow line region. Similarly, such a FWHM is high for most starburst galaxies, although such values have been observed in some (ultra) luminous infrared galaxies (Arribas et al. 2014). Considering all the evidence, we exclude an AGN as the source of the narrow emission lines and favour an origin in star formation.

4.2 Host galaxy star light subtraction and N Bowen fluorescence lines

After we corrected the observed spectra for the contribution of the host stellar light, we do not detect the N lines associated with the Bowen fluorescence lines in any of the spectra of our follow-up campaign. We carefully inspected the spectra of AT 2019dsg to investigate whether the Bowen blend is present or not. As an example, we plot the line fit to the Hδ to Hβ region of the EFOSC2 spectrum of 2019 June 08 before the host galaxy star light is subtracted in Fig. 19. The spectrum shows an emission line at ∼4050 Å and an additional broad component between Hγ and He II. These lines have been associated with N III lines due to the Bowen fluorescence mechanism (Bowen 1934, 1935): the line at 4050 Å as the blend of two N III lines (at 4097 and 4104 Å, shifted by ∼50 Å or 3700 km s^{-1}), while the broad component at 4500 Å can be considered as a blend of many lines (see Steeghs & Casares 2002 for a list of Bowen fluorescence lines at these wavelengths). These emission lines were also identified in van Velzen et al. (2020), leading to the classification of AT 2019dsg as a 'TDE-Bowen'. However, after the host galaxy subtraction process, both of these emission features are not detected in the spectra (see e.g. Fig. 9).

Emission lines due to the Bowen fluorescence have previously been identified in other TDEs: iPTF15af (Blagorodnova et al. 2019), AT2018dyb (Leloudas et al. 2019), ASASSN-14li (Holoien et al. 2016; Prieto et al. 2016), iPTF16fnl (Onori et al. 2019), and AT2019qiz (Nicholl et al. 2020). iPTF15af and AT2018dyb were found in non-active galaxies, while the host galaxies of iPTF16fnl, ASASSN-14li, and AT2019qiz may harbour an AGN. For iPTF15af, iPTF16fnl, and AT2019qiz, host galaxy subtraction was performed on the spectra, while for AT2018dyb and ASASSN-14li this was not the case (the lines were very strong in these events). The subtraction for iPTF15af was performed by fitting a late time spectrum to the source spectrum. In the case of AT2019qiz, the host subtraction was performed by creating a synthetic host galaxy spectrum using

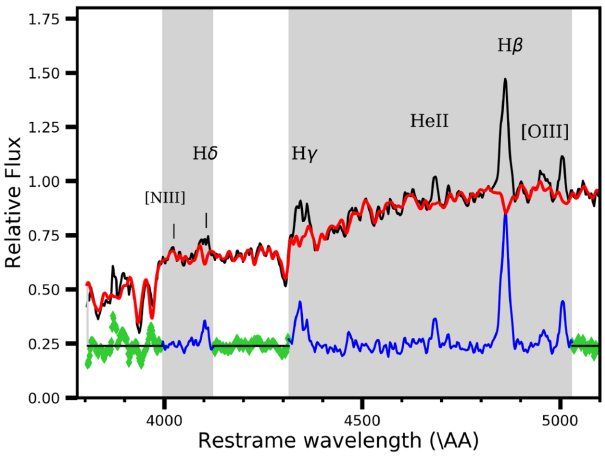

Figure 20. Zoom in of the Hδ–Hβ region on the late time TNG spectrum (+391 d). In black, the source spectrum; in red, the convolved stellar library (the PPXF best-fitting host galaxy synthetic spectrum); in green and blue, the subtracted spectrum. The grey vertical bands indicate the regions of the spectrum excluded from the fit. The Hδ–Hβ region is almost completely masked during the fit, while the rest of the spectrum, except for the Hα line, is considered for the template fitting.

stellar population synthesis models and subtracting it from the source spectrum (this, similarly to our case, removes the stellar contribution). Finally, for iPTF16fnl, a method similar to ours was employed. For the low resolution spectra, they used PPXF to scale a late time host galaxy spectrum to the source spectra to subtract it, while for their X-shooter spectra, they employed the PHOENIX library to create a synthetic host spectrum.

As a check on our host star light subtraction procedure, we also perform the subtraction of the host galaxy stellar component using the late-time TNG spectrum (391 d after the peak of the light curve) to build our synthetic host spectrum. For this spectrum, we use the MILES library (Sánchez-Blázquez et al. 2006; Falcón-Barroso et al. 2011), which consists of ∼1000 stellar spectra covering the 3525–7500 Å wavelength range with a resolution of 2.5 Å. Using PPXF, we first build the synthetic host spectrum and then we scale it to each spectrum of our follow-up campaign and subtract it. The scaling is necessary to account for variable slit losses in the data taking and for the different resolution of the detectors. In Fig. 20, we show the blue part of the observed late-time TNG spectrum, the best-fitting results of the PPXF procedure, i.e. the synthetic host galaxy stellar light, and the residuals. The regions with relevant emission lines, including the wavelength range associated with potential N III Bowen fluorescence features are excluded from the fit. The results of the spectral analysis on these newly subtracted spectra (including the disappearance of the N III lines and the results of the line fit) were consistent within errors with the results presented in Section 3.5. It is interesting to compare our AT 2019dsg results with those of iPTF16fnl obtained by Onori et al. (2019): the spectrum used for the host subtraction in iPTF16fnl also contained a weak N III 4100 Å host galaxy line, but nevertheless the Bowen line was clearly present in the subtracted spectra (see fig. 6 of Onori et al. 2019). In all subtracted spectra, iPTF16fnl clearly shows N lines both at 4100 Å and at 4640 Å, also in the X-shooter spectra, on which the host-subtraction procedure was identical to ours. Clearly, the host stellar light subtraction procedure is not responsible for the non-detection of the N Bowen lines in AT 2019dsg.

We therefore associate the presence of these emission lines in our unsubtracted spectra with spectral features originating in the host galaxy. In our synthetic spectrum (in red in Fig. 20) the area between Hδ and Hβ is similar to the spectrum of a green valley galaxy (see fig. 9 of Pan, Kong & Fan 2013 for an example of a green valley spectrum). That green valley galaxy spectrum clearly shows a feature at ∼4020 Å that matches the one observed in our unsubtracted spectra. In addition, the host galaxy spectrum shows a bump in the continuum around 4500 Å, which when left unsubtracted, can explain the erroneous identification of this feature as a blend of Bowen lines caused by TDE emission.

4.3 Radio emission from AT 2019dsg

In discussing the radio properties of AT 2019dsg, we also consider the radio data first published in Stein et al. (2020; also plotted in Fig. 2). The first radio observations of AT 2019dsg started 42 d after discovery (21 d after peak), at which time AT 2019dsg was already detectable at frequencies $\nu \gtrsim 3$ GHz (Fig. 2) and showed an inverted spectrum (the higher the observing frequency, the higher the observed flux density), indicating that the radio emission was in its optically thick phase at all observed frequencies. Over time the radio emission continued to grow at all frequencies, and around day 50 AT 2019dsg started to enter its optically thin phase at frequencies $\gtrsim$15 GHz. Correspondingly, the peak frequency of AT 2019dsg started to shift progressively towards smaller values, and by day ∼160 AT 2019dsg had reached its optically thin phase also at ∼6 GHz. Our e-MERLIN monitoring shows, however, that the radio emission at 5.1 GHz is still rising to its maximum at ∼160 d, indicating that the TDE had not yet entered the optically thin regime at frequencies $\lesssim$5.1 GHz at that time. This result is in agreement with the value of $\nu_{\rm peak} = 5.4 \pm 0.1$ GHz at t = 158 d reported by Stein et al. (2020). The overall radio behaviour is consistent with the evolution of gas emitting synchrotron radiation, the emission at the lower frequencies is self-absorbed. This has also been seen in other TDEs with radio emission, including both TDEs that showed a relativistic jet (e.g. Arp 299B-AT1 Mattila et al. 2018), and those where the relativistic/sub-relativistic nature of the outflow is less clear (e.g. van Velzen et al. 2016; Alexander et al. 2016). Stein et al. (2020) have modelled the radio emission of AT 2019dsg as a synchrotron self-absorbed sub-relativistic outflow that has a continuous injection of fresh relativistic electrons from a central engine. But we note that in the case of the TDE Arp 299B AT1, Mattila et al. (2018) modelled the radio emission with a relativistic jet whose initial population of electrons are continuously re-accelerated. Stein et al. (2020) find that the expansion of the TDE proceeds with a constant speed for the first three epochs, and then suffers an increase in expansion speed at the latest epoch. However, we note that this explanation is not unique and probably model dependent, as the outflow radius is not measured directly. A relativistic jet with a fast core and a slow sheath seems to be able to account for an almost constant expansion (of the fast jet) as well (Mimica et al. 2015), although we defer detailed radio modelling to future work. Similarly, the increase of the expansion speed seen around day 160 for AT 2019dsg can also be explained by a relativistic jet that encounters a medium with a steep density profile, as found by Mattila et al. (2018) for Arp 299B-AT1. The 5.0 GHz radio emission of Arp 299B AT1 peaked at substantially later epochs, more than ∼1000 d after the event. In contrast, ASASSN-14li (e.g. Bright et al. (2018)) and AT2017gbl (Kool et al. 2020), showed their 5.0 GHz emission peaking around 150 d. At the end of our follow-up, the 5.0 GHz emission from AT 2019dsg has still not reached its peak. We stress that a comparison of phases across different TDEs

is not straightforward, as the reference time is defined differently in different works (e.g. time of discovery or time of peak light).

4.4 X-rays: disc cooling?

The X-ray luminosity decays very quickly, decreasing by a factor ∼100 in roughly 50 d, and becomes undetected ∼100 d after peak, although we lack deep late-time *Chandra* or XMM-*Newton* observations (cf. Jonker et al. 2020). To explain such a dramatic decrease, we can invoke several possible mechanisms that can work alone or in conjunction, such as: (i) an increase in absorption in our line of sight to the X-ray emitting region or (ii) cooling of the disc that causes the emission to shift out of the X-ray band, caused by either a general decrease in mass accretion rate, reducing the energy output, or by an increase in the amount of ionized material causing the X-ray photosphere to move out with time.

The observed cooling of the BB temperature in X-ray spectral fits to the NICER data (Fig. 5) suggest that the first mechanism is not at play, as it would make the observed spectrum harder with time. Furthermore, following the TDE unification idea (Dai et al. 2018) the cooling X-ray disc seems to suggest that we are observing the system relatively pole-on. The second mechanism mentioned above could be at play. We see a decrease in temperature over the first 60 d after the light-curve peak. If this cooling continued, the emission shifts out of the X-ray pass band. Indeed, in the last Swift detection (100 d after peak), the photons were all detected below 0.5 keV. The X-ray luminosity seems to follow the Stefan–Boltzmann law (Fig. 6), meaning that the emission from the disc is consistent with a thermal nature.

What is causing this cooling is unclear: potentially the mass accretion rate is dropping, or alternatively, the photosphere is moving out, due to increased presence of ionized material. The BB radius obtained from the modelling of the X-ray spectrum using a BB model, $R = 3.4^{+1.5}_{-0.9} \times 10^{11}$ cm is smaller than the Schwarzschild radius of a $(5.4 \pm 3.2) \times 10^6 M_\odot$ BH, $R_S = (1.6 \pm 0.9) \times 10^{13}$ cm. While a more edge-on view of the accretion disc could cause the observed emitting region to appear smaller another possible explanation involves the properties of the atmosphere above the accretion disc. Due to a rapid decrease of the opacity with X-ray photon energy due to light element free–free, bound-free, and bound–bound transitions, higher energy X-ray photons are coming from deeper, hotter layers (see for instance the explanation in Zavlin & Pavlov 2002). This effect is seen in quiescent neutron stars (NS), where the presence of an atmosphere causes the emitting radius to be underestimated if modelled with a simple BB (see Kaspi, Roberts & Harding 2010, for a review). It is worth noting that finding BB radii too small for the BH masses is not uncommon in TDEs (e.g. Wevers et al. 2019a).

To better understand the driver behind the decay in X-ray luminosity, we also checked the He II 4686 Å line EW. The He II 4686 Å line is known to be created by photoionization due to (soft) X-ray photons, exhibiting photon-counting properties with a rough correspondence of 1 He II photon emitted for each 0.3–10 keV X-ray photon (Pakull & Angebault 1986; Schaerer, D. et al. 2019). If we compare the photon emission in the X-rays with the He II line EW, we see that the rate of photons emitted in the X-rays is above the amount necessary to explain the detected He II emission line at all epochs where we have data, by a factor of ∼100 at the beginning reducing to a factor ∼2 at the last X-ray detection (100 d after peak). The He II luminosity does not trace the initial dramatic decrease present in the X-ray light curve. Instead, its EW only decreases by a factor ∼4 between 10 and 30 d after peak. This could suggest that the region responsible for the He II emission is (partially) shielded from our line of sight, i.e. the X-ray emission is not 'seen' by all material surrounding the black hole.

There is suggestive evidence for short-term variability in the Swift X-ray data. Other TDEs have shown similar X-ray *flaring* activity (e.g. AT2019ehz, van Velzen et al. 2020 and SDSS J1201, Saxton et al. 2012). This behaviour can, for instance, be explained by a clumpy outflow. Another cause for short-term X-ray variability could be precession of the accretion disc. In such a scenario, when viewed under a large inclination, the disc can intermittently obscure the inner X-ray emitting region. The inclination angle changes due to precession creating the modulation of the light curve on the precession time-scale (Franchini, Lodato & Facchini 2016; Wen et al. 2020). In our case, we favour a more polar line of sight to the system and therefore, we deem the precession scenario as an explanation for the X-ray variability in AT 2019dsg less likely. To explain the variability observed in the Swift light curve (Fig. 4), we could invoke the debris streams caused by the initial disruption of the star. As explored in more detail in Section 4.7, when the star is disrupted, the debris will form self-gravitating streams (Guillochon et al. 2014). If some of these streams are deflected to high enough angles by nodal precession, they could (occasionally) intercept our line of sight to the inner accretion disc, where the X-rays are produced. The variability of the EW of He II (Fig. 14) could be reflecting the variability observed in the Swift X-ray light curve.

At late times (more than 200 d), we start seeing low ionization Fe II emission lines in the spectra. These lines are produced in an optically thick, high-density medium, ionized by X-ray radiation. Low ionization Fe II lines have already been observed in TDEs, as reported in Wevers et al. (2019b), where the authors compare the emergence of these lines to the case of Cataclysmic Variables, where these lines are thought to originate from the surface of the accretion disc. AT 2019dsg is the third UV/optical detected TDE that show these low ionization, optical Fe II emission lines, the other two being AT 2018fyk and ASASSN–15oi (Wevers et al. 2019b). We identify emission from multiplets 37, 38, 42, and 49, which are some of the strongest features also observed in some AGN.

These three Fe-strong TDEs show several similarities in their observed properties. Similar to AT 2018fyk and ASASSN–15oi, AT 2019dsg produced observable X-ray emission (although, note that at the epochs at which we detect the Fe II lines we do not have X-ray data). The Fe lines observed are much narrower than the other TDE lines. As explored below (see Section 4.6), following Roth & Kasen (2018), we hypothesize that in AT 2019dsg the broad lines due to the TDE (He II, Hα, and Hβ) are created in an expanding photosphere that causes the shift of the line centroid and the large FWHM. Therefore, we assume that the Fe lines do not originate in this expanding photosphere, but rather in optically thick clumps of gas. This gas is either pre-existing but only irradiated by X-rays at later times for instance due to disc slimming (Wen et al. 2020) or low-velocity condensations of earlier outflowing material. While the late-time presence of the Fe lines reinforces the idea that there is still X-ray emission, their ionization potential is only a few eV, so that even a 'cool' disc could be sufficient to ionize them.

The X-ray emission from AT 2019dsg is detected from the beginning of the flare, with the first X-ray detection ∼20 d after the optical peak. This, and the subsequent rapid decay of the X-ray luminosity, is opposite to what seen in some other TDEs. For example, ASASSN-15oi (Gezari, Cenko & Arcavi 2017; Holoien et al. 2018), OGLE16aaa (Kajava et al. 2020), and ASASSN-19dj (Hinkle et al. 2021) showed an increase in the X-ray emission at late times, attributed either to a decrease in the optical thickness of material in front of the X-ray emitting region, or to a delayed disc

formation. In the case of ASASSN-15oi, Wen et al. (2020) propose that the late time brightening is due to the slimming of the accretion disc, i.e. a decrease of the scale height of the disc that allows for a more direct view of the inner accretion disc. On the other hand, TDEs like AT 2018fyk (Wevers et al. 2019b), AT 2018hyz (Hung et al. 2020), or AT 2019qiz (Nicholl et al. 2020) all showed evidence for prompt disc formation and X-ray emission with no brightening at later times (the X-ray data of AT 2019qiz cover only ∼100 d after the transient peak light).

The key element to create an accretion disc from the disrupted material is relativistic precession, which is stronger for higher BH mass, deeper disruptions (i.e. disruptions happening closer to the BH) and in the presence of BH spin (depending on the direction of the orbit of the star with respect to the spin vector, see Bonnerot & Stone 2021, for a review). Wevers et al. (2021) attribute the rapid evolution of AT 2018fyk to the higher inferred BH mass: $M_{bh} \sim 5 \times 10^7\,M_\odot$. Indeed, the BH mass for ASASSN-15oi is $\sim 10^6\,M_\odot$, meaning that the lower mass – i.e. a delayed circularization – could explain the brightening of the light curve, but the mass inferred for ASASSN-19dj is $8 \times 10^6\,M_\odot$, higher than the BH masses inferred for AT 2018hyz ($\sim 3 \times 10^6\,M_\odot$), AT 2019qiz ($\sim 3 \times 10^6\,M_\odot$), and AT 2019dsg ($\sim 5 \times 10^6\,M_\odot$), meaning that the difference in BH mass cannot explain alone the differences observed. Most probably, a combination of BH mass, spin, and depth of the disruption all operate together to create a continuum of circularization efficiency. Finally, for lower mass BHs, the TDE luminosity can more easily surpass the Eddington limit, leading to more outflowing material and possibly more obscuration. If the late time brightening is due to a decrease in obscuration, it may take longer for lower-mass BHs to 'clear' the view to the inner accretion disc (X-ray emission from TDEs has been detected years after discovery; see Jonker et al. 2020).

4.5 N Bowen fluorescence lines

Besides showing late-time Fe emission lines, AT 2018fyk, ASASSN–15oi, and AT 2019dsg have another common characteristic: their spectra show no evidence for N III Bowen fluorescence emission. On the other hand, emission features near 3760 Å do appear in all three sources (see e.g. the UVES and ISIS spectra in Fig. 1).

The wavelengths of the 3760 Å features coincide with a group of transitions that can be directly linked to both excited states pumped by the primary Bowen fluorescence process of Oxygen (Bowen 1934). An alternative explanation for these features could be Fe II emission lines from multiplets 120 and 29 (Netzer & Wills 1983), which can be particularly strong due to Fe II self-fluorescence (i.e. wavelengths coincidences between Fe II transitions). However, due to the presence of several transient forbidden transitions of O III (including λ4363, 4960) in the Fe-strong TDEs, we prefer the former explanation.

Why do we observe Bowen O III lines but not the typical N III lines in Fe-strong TDEs? The Bowen fluorescence mechanism is based on a chain of photo-(de)excitations that arise from a strong X-ray ionizing source exciting He II Ly-α photons and a dense medium. The primary fluorescence occurs through Oxygen, whose transitions in turn have resonances that can pump N atoms to excited states. In particular, the O III cascade produces the 2p3s $^3P^0$ state through de-excitations including (among others) the 3760 Å transitions. This unstable state subsequently decays through UV resonance lines (λ 374.432, 374.162 Å) with N III. This results in N III emission near the 4640 Å complex that is the hallmark of Bowen fluorescence, observed in X-ray binaries (McClintock, Canizares & Tarter 1975), novae (Selvelli, Danziger & Bonifacio 2007), planetary nebulae, QSOs (Weymann & Williams 1969), and TDEs (Blagorodnova et al. 2019; Leloudas et al. 2019; Onori et al. 2019).

If resonant line fluorescence is efficient, one would then expect to see N III 4640 Å emission whenever the O III 3760 Å feature is present. However, this does not appear to be the case for Fe-strong TDEs. One straightforward explanation is that the N III 4640 Å emission feature is *hidden* in the Fe II complex. However, the majority of TDEs with Bowen lines have N III 4640 Å emission line fluxes that exceed the O III 3760 Å fluxes (Leloudas et al. 2019). In addition, the 4640 Å feature is clearly visible even next to the dominant He II 4686 Å line. This suggests that the line strength of N III 4640 Å is much lower in Fe-strong TDEs. In other words, the resonant line fluorescence of N III is much less efficient.

Probably the absence of significant N III emission reflects different physical conditions along our line of sight in N- and Fe-strong TDEs. In particular, Selvelli et al. (2007) argued that the key to pumping N III resonance lines is multiple scatterings in an optically thick medium. In optically thin conditions, the probability that an O III resonance photon will directly excite the parent level that results in N III 4640 Å emission is very low. However, if the medium is optically thick, multiple scatterings of the O III photon results in a very high probability of ultimately triggering the N III emission. A more detailed, quantitative analysis to infer the physical properties of the gas will require high SNR spectroscopy of the Bowen lines, including those in the UV part of the spectrum which we are lacking for AT 2019dsg, combined with radiative transfer modelling.

4.6 Broad optical emission lines

It is interesting to consider the evolution of the parameters of the (broad) emission lines detected in AT 2019dsg. The EW and the FWHM of the Hγ line both show a decrease (by a factor ∼2) between 10 and 50 d after peak, a time-scale that is similar to the one over which the blue continuum of the optical spectra decays. More interestingly, the EW of the Hγ line shows a gradual decrease over the whole period of our follow-up campaign. Potentially, there might be two components to that emission line (similarly to Hα and Hβ case): one from the host galaxy and another one from the TDE. However, in the case of the Hγ, we are not able to separate these two components in a narrow and a broad line. The decrease of the EW can be explained by the decay of the broad component arising from the TDE. From 170 d onward, we are probably detecting only the contribution from the host galaxy narrow emission line: the value of the EW is almost a factor 2 lower than the previous data point and does not change any further (see also Table B2). The broad component of Hα and Hβ also is no longer detected at these epochs. If the central wavelength is dominated by the narrow line component originating in the host galaxy, this would also explain the low shift of the central wavelength detected in this line (and in Hδ in the few epochs in which it is constrained). Finally, also the decrease of the ratio between the EW of the Hγ and that of the narrow Hβ (Fig. 16) could be explained by the Hγ having these two components.

The evolution of the He II is also interesting: it is the only line to show a consistent blueshift with respect to the restframe wavelength, and this blueshift is increasing in the last two epochs. The amplitude of this blueshift is in line with the velocity of the radio outflow derived in Stein et al. (2020), which is also increasing around 150 d after peak. The FWHM of the He II also increases at the same time. This could mean that the He II line originates in expanding gas that traces the outflow that could be responsible for the radio emission as well. Its FWHM is then partly determined by electron scattering (Roth & Kasen 2018) and partly by differences in the outflow velocities projected on to our line of sight of the He II emitting gas. The broad components of Hα and Hβ have FWHMs with similar or greater values compared to He II. They could also originate from an

expanding shell of gas. Also the velocity shift of the broad base of Hα has a value similar to the one of He II. Unfortunately, the broad Hα and Hβ were not detected at the last two epochs when the blueshift of the He II line increases. The scenario of expanding material, where X-ray radiation is reprocessed and the broad optical lines are emitted, is similar to the one discussed in Nicholl et al. (2020) for the TDE AT 2019qiz.

4.7 High resolution spectroscopy and absorption lines

In our follow-up campaign of AT 2019dsg, we obtained two medium resolution spectra (ISIS and X-shooter) and one high resolution spectrum (UVES). In these spectra, we see evidence for absorption lines superimposed on the broad emission lines: in both the X-shooter (Fig. 11) and ISIS (Fig. 12) spectra, the Hγ and He II lines show absorption lines. The UVES spectrum (Fig. 17) also provides suggestive evidence for the presence of several absorption lines superimposed on the Hβ line. Unfortunately, the SNR of the UVES spectrum is too low to establish the presence of these potential absorption lines beyond doubt. The spectrum does show evidence that the overall line shape may deviate from a simple Gaussian profile. The Hβ line shows a flat top. Deviations from a Gaussian profile of the broad emission lines of a TDE have been seen before in the literature, with lines showing double peaks and box-shaped profiles (Short et al. 2020).

We thoroughly checked our synthetic host spectrum for features that could artificially create the absorption lines detected in the Hγ and He II lines, during the host-subtraction procedure, but found none. The absorption lines could be due to the host galaxy. On one hand, if this were the case, we would expect the line parameters to not change between the two spectra, especially since they are separated by just 7 d (the line parameters are reported in Table 4). Indeed, the line parameters are consistent to within uncertainties. On the other hand, these lines are present in the spectra after we removed the stellar component, disfavouring such an origin. We check for absorption from diffuse atmospheric bands (DIBs), finding that only the absorption feature in He II at 4660 Å could potentially be explained by the DIB at 4659.8 Å (Hobbs et al. 2008).

When a star is disrupted, the debris may form strongly self-gravitating streams (Guillochon et al. 2014). What we could be seeing is absorption lines caused by such streams, where the different orbital motions and projected velocities of these different streams cause the variation of the width of the lines. To have this, we would need some of the self-gravitating streams to be deflected by large angles, while the bulk of the disrupted material circularizes into an accretion disc, as we deem it likely that the disc is observed under a low inclination angle. Detecting these streams could be an indicator of the BH spin: in fact, to produce the detected absorption lines, the streams have to be somewhat long-lived (in our case, for at least $\sim$120 d). This happens if the streams do not self intersect during their orbital motion. As suggested in Guillochon & Ramirez-Ruiz (2015), the relativistic precession induced by the BH spin can deflect the streams from the original orbital plane, thus avoiding their intersection. This effect is more pronounced for retrograde orbits (Hayasaki, Stone & Loeb 2016) than for prograde ones (Liptai et al. 2019).

As discussed in Section 4.4, we expect the circularization process to be quick, giving rise to prompt accretion and thus luminous X-ray emission. Can these streams be present while active accretion is ongoing? From the simulations of Guillochon & Ramirez-Ruiz (2015), the effect of the BH spin is to introduce a delay between the disruption of the star and the onset of the flare, due to deflection of the stream out of the orbital plane of the star prior to disruption, such that stream self-crossing is delayed. This does not necessarily influence the 'promptness' of the flare; i.e. the creation of the accretion disc can still be quick, once the disrupted material has slammed into itself and lost angular momentum. Moreover, while the 'head' of the stream is settling into a disc, the rest of the stream – that has been stretched out due to the disruption process – is still orbiting around the BH at various deflection angles (see fig. 2 of Guillochon & Ramirez-Ruiz 2015) and can still intercept our line of sight while the disc has formed. What remains unclear is if the deflected stream can be long (lived) enough to still encounter our line of sight at $\sim$120 d after peak. The amount of mass bound to the BH after the disruption and the amount of vertical compression of the stream (e.g. due to magnetic fields, Bonnerot et al. 2017) are probably determining factors for this.

We note that in Leloudas et al. (2019), a search for such absorption features in their UVES spectra is presented, without finding any absorption line due to the TDE.

In the future, employing high resolution spectrographs and developing physical models that account for the fine structure observed could be paramount to obtain a more thorough picture of the dynamics of the debris stream, the eventual formation of the accretion disc and to infer the spin of the BH.

5 SUMMARY

We present results of a spectroscopic monitoring campaign of the TDE AT2019dsg. We perform a detailed analysis of the emission line content and evolution at optical wavelengths, using 26 spectra covering almost 400 d after the light-curve peak. Combining these results with other multiwavelength information, including radio interferometric observations and X-ray and UV measurements, we attempt to explain the multiwavelength observed properties and their evolution in a coherent manner.

(i) The TDE is X-ray bright, but the X-ray luminosity rapidly decays and becomes undetectable in less then 200 d. This rapid decline can be explained with a cooling disc.

(ii) In line with Stein et al. (2020), we suggest that an outflow is powered by the accretion flow and the outflow is responsible for the optical (line) emission. The emission lines, particularly He II, trace the outflow velocity (which, as modelled in Stein et al. 2020, increases between 100 and 160 d after peak). We therefore propose that the emission lines are formed in this expanding medium.

(iii) Our e-MERLIN radio observations show that the emission is still increasing at 5.1 GHz, in contrast with radio observations at higher frequencies, which show a clear decreasing trend. This indicates that the TDE is still optically thick at $t \sim 200$ d for $\nu \lesssim 5.1$ GHz. While Stein et al. (2020) interpreted their radio observations as being due to a sub-relativistic outflow, we warn that a relativistic jet with a fast core and a slow sheath could possible also explain the radio observations (see e.g. Mimica et al. 2015) and, advocating a change in the density profile, the apparent increase in the expansion speed around day 160.

(iv) At later times, more than 200 d after peak, low ionization Fe emission lines appear. We do not have X-ray data at these epochs, but the presence of the Fe lines indicates the continued presence of an ionizing continuum source.

(v) We show that after carefully subtracting the host galaxy light, the features previously identified as N III Bowen fluorescence lines by van Velzen et al. (2020) disappear. This underlines the importance of performing host galaxy subtraction for the spectral study of TDEs.

(vi) We discuss the similarities between the Fe-strong TDEs in terms of the presence/absence of Fe and N Bowen fluorescence lines.

(vii) In our medium/high resolution spectra, we see absorption lines that could be due to the self-gravitating debris streams, caused by the disruption of the star, intercepting our line of sight. High resolution spectroscopy may play a big role in the future for understanding the dynamics of the debris stream in TDEs.

ACKNOWLEDGEMENTS

We thank the anonymous referee for the constructive remarks on this manuscript. GC and PGJ acknowledge support from European Research Council (ERC) Consolidator Grant 647208. TW is funded by ERC grant 320360 and by European Commission grant 730980. This research was made possible through the use of the AAVSO Photometric All-Sky Survey (APASS), funded by the Robert Martin Ayers Sciences Fund and NSFAST-1412587. We acknowledge the use of public data from the *Swift* data archive. We thank P. M. Vreeswijk for the data reduction of the UVES spectrum. This paper includes data obtained with the William Herschel Telescope (proposal IDs: W19B/P7, W19A/N3) as well as observations made with the Italian Telescopio Nazionale Galileo (TNG) operated on the island of La Palma by the Isaac Newton Group of Telescopes and the Fundación Galileo Galilei of the INAF (Istituto Nazionale di Astrofisica) at the Spanish Observatorio del Roque de los Muchachos of the Instituto de Astrofisica de Canarias. Based on observations collected at the European Organisation for Astronomical Research in the Southern Hemisphere under ESO programmes 1103.D-0328 "advanced Public ESO Spectroscopic Survey for Transient Objects" (ePESSTO+). GL was supported by a research grant (19054) from VILLUM FONDEN. D.M.-S. acknowledges support from the ERC under the European Union's Horizon 2020 research and innovation programme (grant agreement no. 715051; Spiders). JM acknowledges financial support from the State Agency for Research of the Spanish MICIU through the "Center of Excellence Severo Ochoa" award to the Instituto de Astrofísica de Andalucía (SEV-2017-0709) and from the grant RTI2018-096228-B-C31 (MICIU/FEDER, EU). IA is a CIFAR Azrieli Global Scholar in the Gravity and the Extreme Universe Program and acknowledges support from that program, from the European Research Council (ERC) under the European Union's Horizon 2020 research and innovation program (grant agreement number 852097), from the Israel Science Foundation (grant numbers 2108/18 and 2752/19), from the United States – Israel Binational Science Foundation (BSF), and from the Israeli Council for Higher Education Alon Fellowship. TWC acknowledges the EU Funding under Marie Skłodowska-Curie grant H2020-MSCA-IF-2018-842471. TMB was funded by the CONICYT PFCHA / DOCTORADOBECAS CHILE/2017-72180113. MN is supported by a Royal Astronomical Society Research Fellowship. FO acknowledges the support of the GRAWITA/PRIN-MIUR project: The new frontier of the Multi-Messenger Astrophysics: follow-up of electromagnetic transient counterparts of gravitational wave sources.

DATA AVAILABILITY

All data will be made available in a reproduction package uploaded to Zenodo.

REFERENCES

Alexander K. D., Berger E., Guillochon J., Zauderer B. A., Williams P. K. G., 2016, ApJ, 819, L25
Alexander K. D., van Velzen S., Horesh A., Zauderer B. A., 2020, Space Sci. Rev., 216, 81
Arcavi I. et al., 2014, ApJ, 793, 38
Arnaud K. A., 1996, in Jacoby G. H., Barnes J., eds, ASP Conf. Ser., Vol. 101, Astronomical Data Analysis Software and Systems V. Astron. Soc. Pac., San Francisco, CA, USA, p. 17
Arribas S., Colina L., Bellocchi E., Maiolino R., Villar-Martín M., 2014, A&A, 568, A14
Baldwin J. A., Phillips M. M., Terlevich R., 1981, PASP, 93, 5
Ballester P., Modigliani A., Boitquin O., Cristiani S., Hanuschik R., Kaufer A., Wolf S., 2000, The Messenger, 101, 31
Blagorodnova N. et al., 2017, ApJ, 844, 46
Blagorodnova N. et al., 2019, ApJ, 873, 92
Bonnerot C., Lu W., 2020, MNRAS, 495, 1374
Bonnerot C., Stone N. C., 2021, Space Sci. Rev., 217, 16
Bonnerot C., Price D. J., Lodato G., Rossi E. M., 2017, MNRAS, 469, 4879
Bowen I. S., 1934, PASP, 46, 146
Bowen I. S., 1935, ApJ, 81, 1
Bright J. S. et al., 2018, MNRAS, 475, 4011
Brown T. M. et al., 2013, PASP, 125, 1031
Cappellari M., 2017, MNRAS, 466, 798
Dai L., McKinney J. C., Roth N., Ramirez-Ruiz E., Miller M. C., 2018, ApJ, 859, L20
Davenport J., de Val-Borro M., Wilkinson T. D., 2016, pydis: Possibly useful. https://doi.org/10.5281/zenodo.58753
Evans C. R., Kochanek C. S., 1989, ApJ, 346, L13
Falcón-Barroso J., Sánchez-Blázquez P., Vazdekis A., Ricciardelli E., Cardiel N., Cenarro A. J., Gorgas J., Peletier R. F., 2011, A&A, 532, A95
Ferrarese L., Ford H., 2005, Space Sci. Rev., 116, 523
Filippenko A. V., 1982, PASP, 94, 715
Franchini A., Lodato G., Facchini S., 2016, MNRAS, 455, 1946
French K. D., Arcavi I., Zabludoff A., 2016, ApJ, 818, L21
Freudling W., Romaniello M., Bramich D. M., Ballester P., Forchi V., García-Dabló C. E., Moehler S., Neeser M. J., 2013, A&A, 559, A96
Gehrels N. et al., 2004, ApJ, 611, 1005
Gendreau K. C. et al., 2016, in Space Telescopes and Instrumentation 2016: Ultraviolet to Gamma Ray, Vol. 9905. SPIE Conference Proceedings, Cardiff, UK, p. 99051H
Gezari S., Cenko S. B., Arcavi I., 2017, ApJ, 851, L47
Guillochon J., Ramirez-Ruiz E., 2015, ApJ, 809, 166
Guillochon J., Manukian H., Ramirez-Ruiz E., 2014, ApJ, 783, 23
Gültekin K. et al., 2009, ApJ, 698, 198
Hayasaki K., Stone N., Loeb A., 2016, MNRAS, 461, 3760
Henden A. A., 2019, J. Am. Assoc. Var. Star Obs., 47, 130
HI4PI Collaboration et al., 2016, A&A, 594, A116
Hills J. G., 1975, Nature, 254, 295
Hinkle J. T. et al., 2021, MNRAS, 500, 1673
Hobbs L. M. et al., 2008, ApJ, 680, 1256
Holoien T. W. S. et al., 2016, MNRAS, 455, 2918
Holoien T. W. S., Brown J. S., Auchettl K., Kochanek C. S., Prieto J. L., Shappee B. J., Van Saders J., 2018, MNRAS, 480, 5689
Hung T. et al., 2020, ApJ, 903, 31
Husser T. O., Wende-von Berg S., Dreizler S., Homeier D., Reiners A., Barman T., Hauschildt P. H., 2013, A&A, 553, A6
Jonker P. G., Stone N. C., Generozov A., van Velzen S., Metzger B., 2020, ApJ, 889, 166
Jordi K., Grebel E. K., Ammon K., 2006, A&A, 460, 339
Kajava J. J. E., Giustini M., Saxton R. D., Miniutti G., 2020, A&A, 639, A100
Kaspi V. M., Roberts M. S. E., Harding A. K., 2010, Isolated neutron stars. Cambridge University Press, Cambridge, UK, p. 279
Kausch W. et al., 2015, A&A, 576, A78
Kewley L. J., Heisler C. A., Dopita M. A., Lumsden S., 2001, ApJS, 132, 37
Komossa S., 2002, in Gilfanov M., Sunyeav R., Churazov E., eds, Lighthouses of the Universe: The Most Luminous Celestial Objects and Their Use for Cosmology. Springer, Berlin, Heidelberg, p. 436
Kool E. C. et al., 2020, MNRAS, 498, 2167
Leloudas G. et al., 2016, Nat. Astron., 1, 0002
Leloudas G. et al., 2019, ApJ, 887, 218
Liptai D., Price D. J., Mandel I., Lodato G., 2019, preprint (arXiv:1910.10154)
Mattila S. et al., 2018, Science, 361, 482
McClintock J. E., Canizares C. R., Tarter C. B., 1975, ApJ, 198, 641

McConnell N. J., Ma C.-P., 2013, ApJ, 764, 184
McCully C. et al. , 2018, Lcogt/Banzai: Initial Release. doi:10.5281/zenodo.1257560
McMullin J. P., Waters B., Schiebel D., Young W., Golap K., 2007, CASA Architecture and Applications. Astronomical Society of the Pacific, San Francisco, CA, USA, p. 127
Mimica P., Giannios D., Metzger B. D., Aloy M. A., 2015, MNRAS, 450, 2824
Netzer H., Wills B. J., 1983, ApJ, 275, 445
Newville M., Stensitzki T., Allen D. B., Ingargiola A., 2014, LMFIT: Non-Linear Least-Square Minimization and Curve-Fitting for Python. https://doi.org/10.5281/zenodo.11813
Nicholl M. et al., 2019a, MNRAS, 488, 1878
Nicholl M. et al., 2019b, Astron. Telegram, 12752, 1
Nicholl M. et al., 2020, MNRAS, 499, 482
Nordin J., Brinnel V., Giomi M., Santen J. V., Gal-Yam A., Yaron O., Schulze S., 2019, Transient Name Serv. Discov. Rep., 2019-615, 1
Onori F. et al., 2019, MNRAS, 489, 1463
Pakull M. W., Angebault L. P., 1986, Nature, 322, 511
Pan Z., Kong X., Fan L., 2013, ApJ, 776, 14
Piran T., Svirski G., Krolik J., Cheng R. M., Shiokawa H., 2015, ApJ, 806, 164
Planck Collaboration, 2014, A&A, 571, A16
Prieto J. L. et al., 2016, ApJ, 830, L32
Prugniel P., Soubiran C., 2001, A&A, 369, 1048
Rees M. J., 1988, Nature, 333, 523
Roth N., Kasen D., 2018, ApJ, 855, 54
Sánchez-Blázquez P. et al., 2006, MNRAS, 371, 703
Saxton R. D., Read A. M., Esquej P., Komossa S., Dougherty S., Rodriguez-Pascual P., Barrado D., 2012, A&A, 541, A106
Schaerer D., Fragos T., Izotov Y. I., 2019, A&A, 622, L10
Schawinski K. et al., 2014, MNRAS, 440, 889
Schlafly E. F., Finkbeiner D. P., 2011, ApJ, 737, 103
Selvelli P., Danziger J., Bonifacio P., 2007, A&A, 464, 715
Shiokawa H., Krolik J. H., Cheng R. M., Piran T., Noble S. C., 2015, ApJ, 804, 85
Short P. et al., 2020, MNRAS, 498, 4119
Smartt S. J. et al., 2015, A&A, 579, A40
Smette A. et al., 2015, A&A, 576, A77
Steeghs D., Casares J., 2002, ApJ, 568, 273
Stein R., Franckowiak A., Necker J., Gezari S., Velzen S. v., 2019a, Astron. Telegram, 13160, 1
Stein R., Franckowiak A., Necker J., Gezari S., van Velzen S., Ztf Collaboration, Growth Collaboration, 2019b, GRB Coord. Netw., 25929, 1
Stein R. et al., 2020, preprint (arXiv:2005.05340)
Stern D. et al., 2012, ApJ, 753, 30
Stone N. C., Metzger B. D., 2016, MNRAS, 455, 859
Tody D., 1986, in Crawford D. L., ed., Proc. SPIE, Vol. 627, Instrumentation in astronomy VI. SPIE, Bellingham, p. 733
Valenti S. et al., 2014, MNRAS, 438, L101
van Velzen S. et al., 2016, Science, 351, 62
van Velzen S. et al., 2020, ApJ, 908, 4
Vernet J. et al., 2011, A&A, 536, A105
Wen S., Jonker P. G., Stone N. C., Zabludoff A. I., Psaltis D., 2020, ApJ, 897, 80
Wevers T., 2020, MNRAS, 497, L1
Wevers T., van Velzen S., Jonker P. G., Stone N. C., Hung T., Onori F., Gezari S., Blagorodnova N., 2017, MNRAS, 471, 1694
Wevers T. et al., 2019a, MNRAS, 487, 4136
Wevers T. et al., 2019b, MNRAS, 488, 4816
Wevers T. et al., 2021, preprint (arXiv:2101.04692)
Weymann R. J., Williams R. E., 1969, ApJ, 157, 1201
Wyrzykowski Ł. et al., 2017, MNRAS, 465, L114
Zavlin V. E., Pavlov G. G., 2002, in Becker W., Lesch H., Trümper J., eds, Neutron Stars, Pulsars, and Supernova Remnants. MPE, Garching, DE, p. 263

APPENDIX A: FLOYDS SPECTRA

Table A1. FLOYDS spectroscopic observations.

MJD[(1)] (d)	Phase[(2)] (d)	UTC Date	Exposure time (s)	Slit (arcsec)
58628.73	+26	2019 May 25	3600	2.0
58645.65	+43	2019 June 11	3600	2.0
58661.72	+59	2019 June 27	3600	2.0
58683.66	+81	2019 July 19	3600	2.0
58696.65	+94	2019 Aug 01	3600	2.0
58712.49	+109	2019 Aug 17	3600	2.0
58735.55	+132	2019 Sep 09	3600	2.0
58748.41	+145	2019 Sep 22	3600	2.0
58766.46	+163	2019 Oct 10	3600	2.0
58779.35	+176	2019 Oct 23	3600	2.0

[(1)] Modified Julian Day of observations; [(2)] calculated with respect to the peak of the light curve, MJD 58603.1.

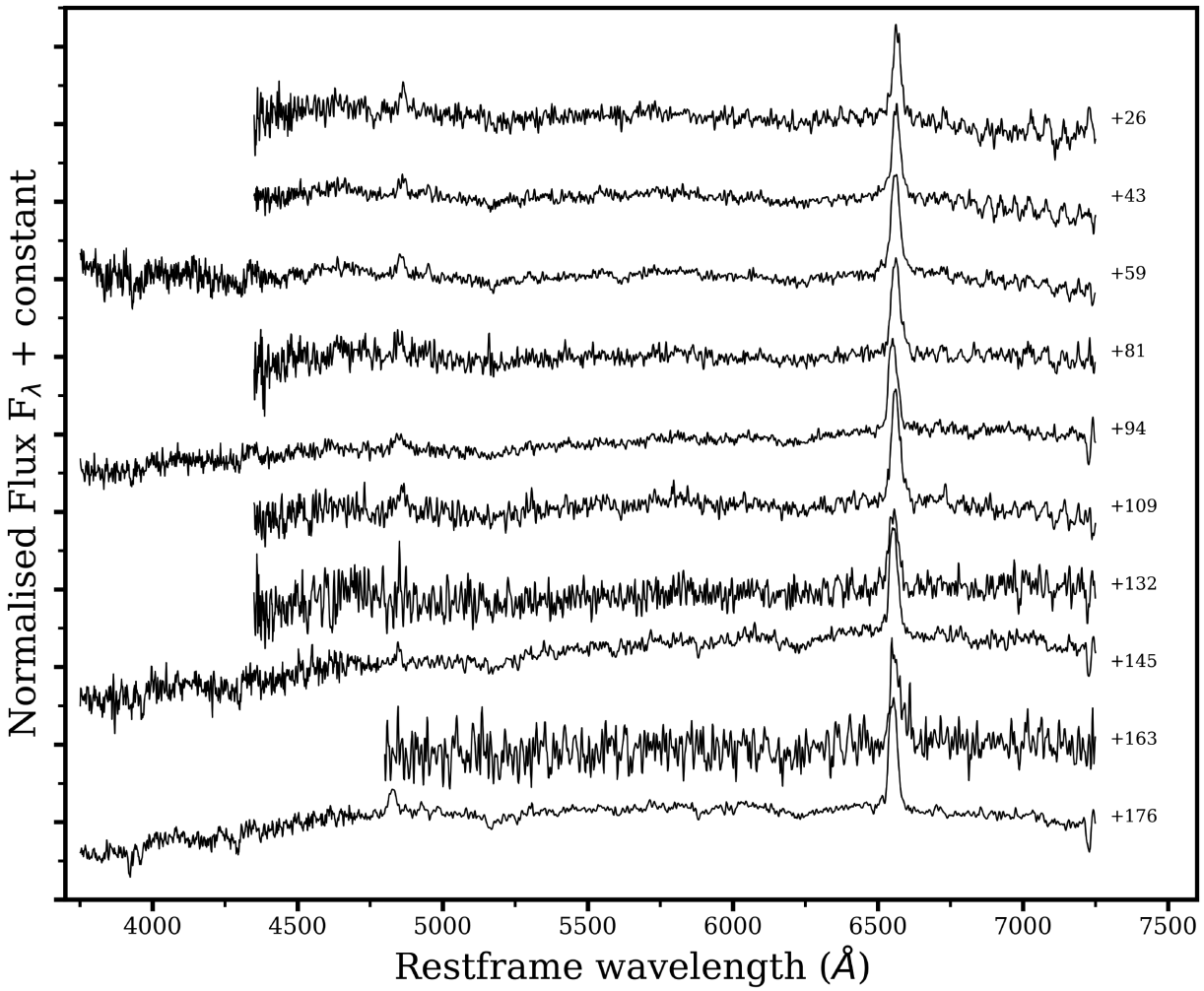

Figure A1. Sequence of spectra taken with the FLOYDS spectrograph. For each spectrum, the phase with respect to the peak light (MJD 58603.1) is reported on the right. For plotting purposes, all spectra have been divided by their median value.

APPENDIX B: LINE-FITTING RESULTS

Table B1. FWHM of the emission lines, in km s^{-1} as measured from our spectra at epoch given by the Modified Julian Date in the first column, corrected for instrumental broadening. With ··· we indicate an epoch in which the line in question could not be fit.

MJD[(1)]	Phase[(2)]	Hδ	Hγ	He II	Hβ broad	Hα broad	Hβnarrow	Hα narrow
58616.36	+13	3880 ± 340	3560 ± 280	9850 ± 370	5800 ± 740	11 970 ± 1010	1110 ± 110	920 ± 60
58631.13	+28	4630 ± 200	3020 ± 170	5790 ± 290	2720 ± 740	8840 ± 670	1010 ± 220	1020 ± 70
58638.28	+35	···	···	7610 ± 660	4310 ± 760	7540 ± 880	1180 ± 210	1170 ± 30
58642.35	+39	4020 ± 310	2290 ± 230	7610 ± 430	3910 ± 870	5630 ± 420	1100 ± 160	960 ± 60
58644.32	+41	3790 ± 230	2880 ± 210	6980 ± 370	3920 ± 840	6810 ± 430	1100 ± 130	750 ± 60
58655.19	+52	···	2440 ± 420	7260 ± 810	15 080 ± 3310	14 100 ± 930	1400 ± 120	1060 ± 70
58656.12	+53	···	2170 ± 260	8940 ± 770	5800 ± 530	11 110 ± 730	1150 ± 110	1070 ± 70
58657.09	+54	···	1970 ± 190	6980 ± 420	5750 ± 750	12 140 ± 740	1220 ± 90	1050 ± 70
58658.14	+55	···	2360 ± 180	10 760 ± 360	5450 ± 810	8740 ± 690	850 ± 90	1060 ± 70
58676.19	+73	···	2040 ± 180	8720 ± 420	6640 ± 450	12 490 ± 710	1160 ± 90	1100 ± 70
58678.10	+75	···	2710 ± 240	8050 ± 500	11 200 ± 1330	13 200 ± 890	1310 ± 90	1120 ± 80
58689.25	+86	3040 ± 400	2590 ± 210	10 300 ± 440	4830 ± 850	11 450 ± 1370	1320 ± 130	1020 ± 70
58690.11	+87	···	2190 ± 300	6930 ± 510	3950 ± 950	12 580 ± 1040	1210 ± 110	1110 ± 80
58692.12	+89	···	2310 ± 180	7740 ± 340	8150 ± 780	12150 ± 710	1280 ± 90	1150 ± 70
58710.94	+108	···	···	6320 ± 470	20 100 ± 9500	10 210 ± 850	1390 ± 130	1170 ± 80
58715.88	+113	···	2460 ± 180	7410 ± 380	5780 ± 450	11 910 ± 1250	1210 ± 90	1170 ± 70
58717.00	+114	···	2270 ± 200	7300 ± 410	8000 ± 760	12 570 ± 970	1370 ± 90	1180 ± 70
58717.89	+115	···	1890 ± 110	6310 ± 270	4710 ± 220	···	1220 ± 40	···
58724.14	+121	···	2160 ± 36	6370 ± 110	3570 ± 150	···	1190 ± 20	···
58733.93	+131	···	3280 ± 550	7440 ± 1020	5470 ± 1030	10140 ± 1010	1210 ± 150	1180 ± 80
58735.96	+133	···	2420 ± 290	7630 ± 600	8610 ± 1110	13100 ± 1110	1290 ± 100	1170 ± 80
58777.02	+174	···	2510 ± 300	11 730 ± 780	···	···	1800 ± 150	1100 ± 60
58808.04	+205	···	2200 ± 390	13 000 ± 1310	···	···	1520 ± 90	···
58824.83	+222	···	···	···	···	···	···	1260 ± 50
58827.82	+224	···	···	···	···	···	···	1230 ± 60
58994.00	+391	···	1860 ± 160	···	···	···	1190 ± 60	1170 ± 50

(1) Modified Julian Date of the observations, (2) days passed from the peak of the light curve, MJD 58603.1.

Table B2. EW of the emission lines, in Å. With ··· we indicate an epoch in which the line in question could not be fit.

MJD[(1)]	Phase[(2)]	Hδ	Hγ	He II	Hβ broad	Hα broad	Hβ narrow	Hα narrow
58616.36	+13	9.0 ± 1.0	10.8 ± 1.1	44.6 ± 2.2	15.1 ± 3.1	33.5 ± 3.6	11.1 ± 1.2	43.0 ± 1.0
58631.13	+28	13.2 ± 0.7	8.5 ± 0.6	14.2 ± 1.0	5.8 ± 4.3	23.6 ± 2.5	6.6 ± 2.1	36.8 ± 1.1
58638.28	+35	···	···	17.6 ± 1.9	8.7 ± 2.6	15.6 ± 2.6	4.4 ± 1.0	29.8 ± 1.2
58642.35	+39	9.4 ± 0.9	5.8 ± 0.7	19.3 ± 1.4	7.1 ± 3.4	16.3 ± 2.0	8.4 ± 1.4	26.0 ± 0.9
58644.32	+41	11 ± 0.8	8.0 ± 0.7	18.9 ± 1.3	7.2 ± 3.0	21.9 ± 2.0	9.3 ± 1.2	35.3 ± 0.9
58655.19	+52	···	6.2 ± 1.3	13.4 ± 2.1	24.3 ± 5.9	36.4 ± 3.0	11.2 ± 0.9	37.3 ± 0.8
58656.12	+53	···	7.6 ± 1.1	15.5 ± 1.7	15.7 ± 2.3	35.1 ± 3.0	11.6 ± 0.9	47.4 ± 1.0
58657.09	+54	···	6.8 ± 0.8	14.4 ± 1.1	8.0 ± 1.7	40.8 ± 3.1	12.2 ± 0.6	49.5 ± 1.0
58658.14	+55	···	8.9 ± 0.8	36.8 ± 1.5	6.6 ± 1.5	22.5 ± 2.4	7.5 ± 0.5	47.0 ± 0.9
58676.19	+73	···	6.7 ± 0.6	18.5 ± 1.1	16.5 ± 1.6	39.9 ± 2.9	9.6 ± 0.5	48.2 ± 0.8
58678.10	+75	···	7.5 ± 0.8	16.8 ± 1.2	20.6 ± 2.7	38.9 ± 3.3	9.6 ± 0.5	43.1 ± 1.0
58689.25	+86	4.9 ± 0.8	7.9 ± 0.7	28.5 ± 1.6	8.6 ± 2.9	23.4 ± 3.6	10.3 ± 1.2	38.8 ± 1.1
58690.11	+87	···	5.2 ± 0.9	12.8 ± 1.2	4.3 ± 2.0	32.3 ± 3.5	8.9 ± 0.9	45.6 ± 1.1
58692.12	+89	···	6.9 ± 0.6	17.0 ± 1.1	13.0 ± 1.7	35.1 ± 2.7	11.0 ± 0.5	49.0 ± 0.8
58710.94	+108	···	5.5 ± 2.0	13.1 ± 4.3	37.6 ± 20.0	30.4 ± 3.5	12.9 ± 1.2	50.3 ± 1.2
58715.88	+113	···	8.4 ± 0.7	14.9 ± 1.0	10.6 ± 1.3	22.6 ± 3.1	9.1 ± 0.5	43.7 ± 0.9
58717.00	+114	···	6.1 ± 0.6	12.8 ± 0.9	10.9 ± 1.5	26.7 ± 2.6	8.8 ± 0.4	41.4 ± 0.8
58717.89	+115	···	9.6 ± 1.6	23.0 ± 1.5	20.9 ± 1.6	···	14.3 ± 0.6	···
58724.14	+121	···	7.3 ± 0.2	15.9 ± 0.4	5.8 ± 0.5	···	9.1 ± 0.2	···
58733.93	+131	···	8.1 ± 1.7	13.3 ± 2.4	11.0 ± 3.3	24.9 ± 3.4	9.1 ± 1.1	53.0 ± 1.2
58735.96	+133	···	6.5 ± 0.9	13.9 ± 1.4	12.2 ± 2.1	38.7 ± 4.2	10.9 ± 0.6	61.4 ± 1.5
58777.02	+174	···	4.2 ± 0.6	15.5 ± 1.3	···	···	11.5 ± 0.5	41.1 ± 0.9
58808.04	+205	···	3.4 ± 0.7	14.8 ± 1.9	···	···	10.1 ± 0.6	···
58824.83	+222	···	···	···	···	···	···	45.2 ± 1.0
58827.82	+224	···	···	···	···	···	···	46.7 ± 1.2
58994.00	+391	···	4.6 ± 0.5	···	···	···	13.6 ± 0.5	65.9 ± 2.6

(1) Modified Julian Date of the observations, (2) days passed from the peak of the light curve, MJD 58603.1.

Table B3. Shift with respect to the restframe wavelength of the emission lines, in km s^{-1}. With ··· we indicate an epoch in which the line in question could not be fit. The narrow peaks of Hα and Hβ are not listed, as we assumed they were at the restframe and we used their offset to probe uncertainties in the wavelength calibration.

MJD[(1)]	Phase[(2)]	Hδ	Hγ	He II	Hβ broad[(3)]	Hα broad
58616.36	+13	240 ± 330	170 ± 310	− 1770 ± 320	20 ± 300	− 170 ± 460
58631.13	+28	230 ± 310	630 ± 300	− 1440 ± 320	420 ± 300	− 220 ± 370
58638.28	+35	···	···	− 2410 ± 360	− 200 ± 300	− 1560 ± 460
58642.35	+39	− 460 ± 320	310 ± 310	− 2670 ± 330	− 60 ± 300	− 760 ± 350
58644.32	+41	− 36 ± 310	150 ± 310	− 2250 ± 320	− 100 ± 300	− 380 ± 340
58655.19	+52	···	− 72 ± 340	− 1960 ± 470	− 400 ± 300	− 1820 ± 440
58656.12	+53	···	− 200 ± 310	− 1190 ± 420	− 320 ± 290	− 690 ± 390
58657.09	+54	···	240 ± 300	− 1860 ± 330	− 180 ± 290	− 840 ± 390
58658.14	+55	···	130 ± 300	− 260 ± 320	− 140 ± 290	− 1190 ± 380
58676.19	+73	···	80 ± 300	− 1630 ± 330	− 280 ± 290	− 820 ± 390
58678.10	+75	···	− 100 ± 310	− 2270 ± 370	− 420 ± 290	− 1390 ± 420
58689.25	+86	370 ± 330	480 ± 300	− 2740 ± 340	− 90 ± 300	40 ± 540
58690.11	+87	···	55 ± 320	− 2670 ± 340	− 380 ± 290	− 760 ± 460
58692.12	+89	···	9 ± 300	− 1850 ± 330	− 370 ± 290	− 930 ± 390
58710.94	+108	···	···	− 2350 ± 490	− 450 ± 300	− 600 ± 410
58715.88	+113	···	350 ± 300	− 1590 ± 320	− 150 ± 290	− 2890 ± 550
58717.00	+114	···	69 ± 300	− 1750 ± 330	− 230 ± 290	− 900 ± 440
58717.89	+115	···	240 ± 60	− 2530 ± 70	− 60 ± 60	···
58724.14	+121	···	210 ± 17	− 2250 ± 30	− 460.1 ± 40	···
58733.93	+131	···	620 ± 360	− 1050 ± 460	− 250 ± 300	− 880 ± 450
58735.96	+133	···	330 ± 320	− 1300 ± 370	− 90 ± 290	− 1470 ± 480
58777.02	+174	···	380 ± 320	− 3550 ± 380	···	···
58808.04	+205	···	− 230 ± 330	− 3540 ± 500	···	···
58824.83	+222	···	···	···	···	···
58827.82	+224	···	···	···	···	···
58994.00	+391	···	150 ± 300	···	···	···

[(1)]Modified Julian Date of the observations, [(2)] days passed from the peak of the light curve, MJD 58603.1. [(3)]The central wavelength of the broad Hβ has been tied to the one of the narrow peak during the fitting procedure.

APPENDIX C: PHOTOMETRY DATA

Table C1. Extinction corrected, host subtracted AB magnitudes.

MJD[(1)]	Seeing [arcsec]	w2	m2	w1	U	B	V	g	r
58619.12*	1.9	···	···	···	···	···	17.34 ± 0.20	17.57 ± 0.08	17.53 ± 0.10
58620.71*	2.4	···	···	···	···	17.80 ± 0.12	17.99 ± 0.08	17.64 ± 0.08	···
58620.18	···	15.71 ± 0.05	15.97 ± 0.06	16.24 ± 0.07	16.61 ± 0.16	···	···	···	···
58621.07*	2.4	···	···	···	···	17.68 ± 0.13	18.04 ± 0.08	17.55 ± 0.08	17.86 ± 0.08
58624.08	···	15.81 ± 0.05	15.97 ± 0.06	16.33 ± 0.08	16.91 ± 0.17	16.66 ± 0.10	···	···	···
58627.21	···	15.91 ± 0.05	15.97 ± 0.05	16.42 ± 0.07	16.78 ± 0.16	···	···	···	···
58627.80*	1.9	···	···	···	···	17.70 ± 0.11	17.88 ± 0.08	17.55 ± 0.08	17.62 ± 0.10
58630.32	···	15.96 ± 0.05	15.99 ± 0.05	16.45 ± 0.07	16.76 ± 0.16	···	···	···	···
58633.52	···	15.86 ± 0.06	16.01 ± 0.07	16.51 ± 0.10	16.92 ± 0.18	···	···	···	···
58636.10	···	16.02 ± 0.05	16.30 ± 0.05	16.55 ± 0.07	17.03 ± 0.16	···	···	···	···
58639.27*	2.2	···	···	···	···	···	18.23 ± 0.25	17.88 ± 0.08	17.79 ± 0.10
58639.83	···	16.06 ± 0.04	16.25 ± 0.05	16.51 ± 0.06	17.00 ± 0.15	···	···	···	···
58642.40	···	16.10 ± 0.04	16.24 ± 0.05	16.61 ± 0.06	17.05 ± 0.15	···	···	···	···
58645.32	···	16.14 ± 0.05	16.31 ± 0.06	16.61 ± 0.07	17.13 ± 0.16	···	···	···	···
58647.69*	2.2	···	···	···	···	18.28 ± 0.11	18.36 ± 0.07	17.98 ± 0.07	18.10 ± 0.09
58648.79	···	16.23 ± 0.05	16.34 ± 0.06	16.58 ± 0.07	16.99 ± 0.16	···	···	···	···
58653.58	···	16.32 ± 0.07	16.33 ± 0.07	16.71 ± 0.09	17.18 ± 0.18	···	···	···	···
58655.09*	2.8	···	···	···	···	18.31 ± 0.13	18.99 ± 0.10	18.82 ± 0.11	18.14 ± 0.11
58656.04+	1.1	···	···	···	···	18.70 ± 0.11	18.47 ± 0.09	18.16 ± 0.10	18.23 ± 0.13
58661.07+	1.0	···	···	···	···	18.64 ± 0.11	18.49 ± 0.11	18.25 ± 0.09	18.26 ± 0.14
58661.75*	2.4	···	···	···	···	18.62 ± 0.11	18.78 ± 0.07	18.30 ± 0.07	18.46 ± 0.09
58665.42*	2.4	···	···	···	···	18.78 ± 0.11	18.96 ± 0.07	18.31 ± 0.07	18.65 ± 0.08
58667.10+	1.1	···	···	···	···	18.57 ± 0.11	18.67 ± 0.10	18.21 ± 0.09	18.63 ± 0.12
58672.13+	1.3	···	···	···	···	18.55 ± 0.11	19.02 ± 0.08	18.52 ± 0.08	18.76 ± 0.10
58675.16	···	16.64 ± 0.07	16.87 ± 0.08	17.10 ± 0.10	17.44 ± 0.18	···	···	···	···
58675.95*	2.1	···	···	···	···	19.15 ± 0.11	18.89 ± 0.08	18.46 ± 0.08	18.40 ± 0.09
58680.19	···	16.73 ± 0.06	17.04 ± 0.07	17.18 ± 0.08	17.72 ± 0.17	···	···	···	···
58682.42*	2.9	···	···	···	···	19.25 ± 0.18	19.04 ± 0.12	18.18 ± 0.11	18.28 ± 0.11
58687.00+	1.3	···	···	···	···	18.74 ± 0.11	18.21 ± 0.08	18.67 ± 0.08	19.64 ± 0.08
58689.96*	2.3	···	···	···	···	19.12 ± 0.11	19.00 ± 0.08	18.59 ± 0.07	18.94 ± 0.08
58693.01+	1.4	···	···	···	···	19.23 ± 0.11	19.36 ± 0.09	18.63 ± 0.08	18.85 ± 0.12
58693.60	···	16.89 ± 0.06	17.15 ± 0.08	17.44 ± 0.07	···	···	···	···	···
58695.39	···	17.20 ± 0.09	17.22 ± 0.12	17.65 ± 0.10	···	···	···	···	···
58696.85*	2.4	···	···	···	···	19.42 ± 0.11	19.46 ± 0.08	18.75 ± 0.07	18.97 ± 0.09
58699.09+	1.1	···	···	···	···	19.67 ± 0.11	19.43 ± 0.09	18.88 ± 0.09	19.26 ± 0.12
58699.31	···	17.24 ± 0.07	17.35 ± 0.10	17.68 ± 0.08	···	···	···	···	···
58703.44	···	17.00 ± 0.09	17.44 ± 0.14	17.50 ± 0.10	···	···	···	···	···
58704.12*	2.7	···	···	···	···	···	···	19.10 ± 0.07	19.41 ± 0.09
58705.12+	1.1	···	···	···	···	19.32 ± 0.11	19.54 ± 0.10	18.99 ± 0.10	19.37 ± 0.11
58707.42	···	17.24 ± 0.08	17.40 ± 0.10	17.46 ± 0.08	···	···	···	···	···
58712.80	···	17.49 ± 0.08	17.69 ± 0.11	17.81 ± 0.08	···	···	···	···	···
58712.81*	1.9	···	···	···	···	···	19.43 ± 0.10	19.26 ± 0.09	18.36 ± 0.10
58726.84*	2.6	···	···	···	···	···	20.08 ± 0.07	19.21 ± 0.07	19.75 ± 0.09
58729.28	···	17.66 ± 0.10	···	···	···	···	···	···	···
58731.93	···	17.38 ± 0.11	17.77 ± 0.14	17.90 ± 0.17	17.93 ± 0.22	···	···	···	···
58733.44	···	17.66 ± 0.14	17.66 ± 0.16	17.75 ± 0.18	18.47 ± 0.28	···	···	···	···
58735.39*	3.0	···	···	···	···	···	20.21 ± 0.09	···	19.48 ± 0.10
58761.06	···	17.91 ± 0.12	18.02 ± 0.13	18.01 ± 0.16	18.42 ± 0.24	···	···	···	···
58766.05	···	18.00 ± 0.17	18.34 ± 0.21	18.23 ± 0.23	18.11 ± 0.25	···	···	···	···
58771.43	···	17.94 ± 0.09	18.13 ± 0.10	18.08 ± 0.12	18.17 ± 0.18	···	···	···	···

[(1)]Modified Julian Date of the observations. Epochs marked with * indicate data from Las Cumbres, epochs marked with + indicate data from LT, the rest of the data are taken with *Swift*. For all filters, the extinction correction was done using the values in Schlafly & Finkbeiner (2011) who assume a reddening law with $R_v = 3.1$.

This paper has been typeset from a TEX/LATEX file prepared by the author.